# THE IGNITION DESIGN SPACE
# OF
# MAGNETIZED TARGET FUSION

Irvin R. (Irv) Lindemuth

December 28, 2015

This paper has been accepted for publication in Physics of Plasmas. Since changes may be made prior to publication, this preprint is made available with the understanding that it will not be distributed without the permission of the author. Feedback is always welcome: irvl@att.net.

(this page intentionally left blank)

The Ignition Design Space of Magnetized Target Fusion

Irvin R. Lindemuth
Tucson AZ 85745, USA

The simple magnetized target implosion model of Lindemuth and Kirkpatrick (Nucl. Fusion **23**, 263, 1983) has been extended to survey the potential parameter space in which three types of magnetized targets—cylindrical with axial magnetic field, cylindrical with azimuthal magnetic field, and spherical with azimuthal magnetic field—might achieve ignition and produce large gain at achievable radial convergence ratios. The model has been used to compute the dynamic, time-dependent behavior of many initial parameter sets that have been based upon projected ignition conditions using the quasi-adiabatic and quasi-flux-conserving properties of magnetized target implosions. The time-dependent calculations have shown energy gains greater than 30 can potentially be achieved for each type of target. By example, it is shown that high gain may be obtained at extremely low convergence ratios, e.g., less than 15, for appropriate initial conditions. It is also shown that reaching the ignition condition, i.e., when fusion deposition rates equal total loss rates, does not necessarily lead to high gain and high fuel burn-up. At the lower densities whereby fusion temperatures can be reached in magnetized targets, the fusion burn rate may be only comparable to the hydrodynamic heating/cooling rates. On the other hand, when the fusion burn rates significantly exceed the hydrodynamic rates, the calculations show a characteristic rapid increase in temperature due to alpha particle deposition with a subsequent increased burn rate and high gain. A major result of this paper is that each type of target operates in a different initial density-energy-velocity range. The results of this paper provide initial target plasma parameters and driver parameters that can be used to guide plasma formation and driver development for magnetized targets. The results indicate that plasmas for spherical, cylindrical with azimuthal field, and cylindrical with axial field targets must have an initial density greater than approximately $10^{17}/\mathrm{cm}^3$, $10^{18}/\mathrm{cm}^3$, and $10^{20}/\mathrm{cm}^3$, respectively, implying constraints on target plasma formation research.

## I. INTRODUCTION

Although they may disagree on when, all energy supply experts predict an energy shortage in the future as global demand increases. Controlled thermonuclear fusion is potentially a nearly unlimited source of energy. Unfortunately, promises of fusion energy in the 1960s did not materialize, and there is a cliché that fusion is, and always will be, 30 years in the future.

The global research on fusion has focused primarily on two distinct conventional approaches, magnetic confinement fusion (MCF) and inertial confinement fusion (ICF). These two approaches are embodied in two multi-billion dollar facilities, ITER for MCF and NIF (the National Ignition Facility) for ICF. These two approaches differ in fusion fuel density by a factor of more than $10^{11}$. The fusion fuel density in ITER will be about $10^{14}$ ions/cm$^3$ (mass density $\rho$=4.2 x $10^{-10}$ g/cm$^3$) and the "hot spot" density of a NIF target will be greater than $10^{25}$ ions/cm$^3$ ($\rho$ > 42 g/cm$^3$). Lindemuth and Siemon (L&S-09)[1] have discussed the parameter space of controlled fusion from a fundamental perspective and show that the potential fusion parameter space is, in fact, a continuum between the two extremes of MCF and ICF. They also show that the fuel density in MCF is primarily determined by the MCF goal of steady-state confinement whereas the fuel density in ICF is primarily determined by the energy limitations of existing drivers and by the use of unmagnetized fuel. In fact, because of these constraints, the two conventional approaches have a very limited design space in which to operate.

L&S-09 also suggest that the lowest cost may actually occur at a density that is approximately the geometric mean between MCF and ICF. One approach to accessing the density range between MCF and ICF is the use of an imploding shell, i.e., a liner or pusher, to compress a magnetized plasma to fusion conditions. As currently envisioned, Magnetized Target Fusion (MTF) is a two-step process: (1) formation of a magnetized plasma either within an implodable container or external to the container, in which case the plasma must be injected into the container after formation; and (2) implosion of the shell surrounding the preformed, magnetized plasma.

The idea of magnetized targets has existed for more than five decades. In 1983, Lindemuth and Kirkpatrick (L&K-83)[2] formulated a simple implosion model and performed the first comprehensive survey of the parameter space in which magnetized targets might work. The references in that document serve as a list of earlier work.

MTF is also referred to as Magneto-Inertial Fusion (MIF). Although the term MTF has sometimes been restricted in the literature to the lowest densities and velocities for which magnetized targets are likely to work, the terminology as coined by the author in 1991 was meant to be all-inclusive--if an implosion system has a magnetized target, it is Magnetized Target Fusion. Although L&K-83 emphasized new "islands" in parameter space, L&K-83 also showed that the density spectrum of magnetized targets is continuous from the high density of ICF down to a density that is many orders of magnitude lower.

Lost in history is that the first fusion neutrons produced in the U.S. particle beam fusion program came from a magnetized target imploded by an electron beam machine at Sandia National Laboratory (SNL).[3] These "Φ-targets" were promising and the best available computations at the time showed that high-gain was possible.[4] However, magnetized targets were abandoned in favor of unmagnetized targets, and this abandonment lead to the unfortunate demise of the U.S. electron and light-ion fusion programs because the drivers could not meet the requirements for unmagnetized targets. Other magnetized target approaches did not reach technical maturity and were prematurely terminated as funding was diverted to the conventional approaches.

Advances in plasma formation methods, driver capabilities, diagnostics, computational tools, and theoretical understanding in the last few decades have increased the chances of success in MTF. Due in part to the difficulty of obtaining ignition at NIF, there is a resurgence of interest in magnetized targets. A team led by the Los Alamos National Laboratory (LANL) and Air Force Research Laboratory (AFRL) has been investigating solid liner compression of magnetically confined field-reversed configuration (FRC) plasmas to achieve fusion temperatures.[5] The University of Rochester has introduced seed magnetic fields into the center of targets at the OMEGA laser facility, and compressed those fields by imploding a liner with the OMEGA laser to record values of magnetic field and demonstrated increases in neutron yields, even though the fuel density in the experiments was not optimum.[6]

SNL is developing the MagLIF (Magnetized Liner Inertial Fusion) system, in which a magnetically driven beryllium liner, imploded by SNL's Z-machine, adiabatically compresses a laser-preheated magnetized DT (deuterium-tritium) target plasma. In the very first series of MagLIF experiments, $10^{11}$-$10^{12}$ DD (deuterium-deuterium) fusion neutrons were observed, indicating significant improvement in target performance due to the presence of preheated and magnetized fuel in the target.[7] The experiments also showed a significant DT yield fraction ($\sim 10^{-2}$) from a pure DD fuel, indicating magnetization of the DD fusion-produced tritons.[8] The SNL experiments were prompted by the computations of Slutz et al. (Slutz-10), who give a complete review of the arguments for magnetizing an implodable target.[9]

LANL also leads a team that is exploring a standoff concept of using a spherically convergent array of gun-driven plasma jets to achieve assembly and implosion of a plasma liner (PLX) without the need to destroy material liners or transmission lines on each shot.[10] A private company, General Fusion in Canada, is developing a merging compact toroid plasma source and envisions rep-rated acoustic drivers that would drive a liquid liner through thick liquid walls.[11] The possible advantage of magnetized targets for the NIF have been evaluated computationally.[12]

MAGO efforts in Russia[13] have stimulated international interest in MTF. A fledgling effort is underway in China.[14] NNSA's "Ignition Path Forward" report to Congress clearly makes MagLIF an element of the national ignition campaign.[15] In August 2014, the U.S. Department of Energy Advanced Research Projects Agency (ARPA-E) announced a new "program (that) will focus on intermediate density fusion approaches between low-density, magnetically confined plasmas and high-density, inertially confined plasmas" and initial funding awards have been made.[16] The on-going MTF approaches span implosion time scales ranging from sub-ns to hundreds of μs, an indication of the potential wide-ranging parameter space in which MTF might work.

The status of MTF research in North America—recent progress, research opportunities, and future plans—has recently been reviewed by Wurden et al.[17] As now discussed by many authors, MTF has a number of potential advantages over conventional ICF, including no pulse shaping, lower implosion velocities, higher energy drivers, and longer dwell times. A major advantage of MTF is the potential for convergence ratios much lower than the difficult-to-achieve 35-40 required in ICF.

Because of the plasma formation and driver capabilities available at the time, L&K-83 focused on spherical targets with low kinetic energy and low initial temperature, e.g., 10 kJ and 50 eV, and with closed magnetic field lines. However, L&K-83 noted "a straightforward extension of our work would be the treatment of cylindrical systems with either open or closed magnetic field lines." Subsequently, the model was extended to deuterium–helium fuel and cylindrical geometry with an azimuthal magnetic field and initial results were reported;[18] because the effect of alpha particle deposition was not taken into account, the cylindrical results were not optimistic. Alpha particle deposition without magnetic effects and a "cold fuel" layer were added to the L&K-83 model and high gain was obtained at a "hot spot" density and implosion velocity significantly lower than required for conventional targets.[19] In fact, the hot spot initial density, implosion velocity, and magnetic field for highest spherical target gain ($\rho$ = 4 mg/cm$^3$, $v$ = 10 cm/μs, $B$ = 100 kG) were very close to the parameters determined by the more sophisticated MagLIF cylindrical calculations of Slutz and Vesey (S&V-12).[20]

This paper extends L&K-83 by including additional physics and by addressing cylindrical geometries with both open and closed magnetic field lines. Physics model extensions discussed in this paper include magnetic effects on alpha particle deposition and the thermoelectric effect. Presumably, the model could be extended to more complex geometries for which volumes, surfaces, etc., can be determined as a function of the radius of an imploding shell. A similar model based on an FRC target plasma was developed by Armstrong,[21] who was not able to obtain gains much greater than unity primarily due to excessive plasma length changes and plasma/liner contact.

As with L&K-83, the main purpose of the computations reported here are "to provide a starting point for more comprehensive investigations" by rapidly scanning the potential parameter space. In addition, the simple model provides a learning tool by providing insight into the various competing processes. The model also helps build an intuition about the tradeoffs in MTF, such as driver complexity vs. plasma formation complexity, initial plasma temperature vs. convergence, etc. The model also defines "ballpark" values of initial plasma parameters (e.g., density, temperature, magnetic field, size) and driver parameters (e.g., velocity, energy, convergence) that can be used to guide the development of plasma formation and driver systems. In the same spirit, McBride and Slutz have developed a more complete, semi-analytic model of MagLIF implosions.[22]

This paper surveys the potential ignition parameter space of MTF for cylindrical targets with an axial magnetic field ($B_z$), cylindrical targets with an azimuthal magnetic field ($B_\varphi$), and spherical targets with an azimuthal magnetic field ($B_\varphi$). The ignition space is then used to define initial conditions for time-dependent implosion calculations by invoking the quasi-adiabatic, quasi-flux-conserving properties of MTF implosions. The present work differs somewhat from the approach of L&K-83. L&K-83 chose an energy-to-mass ratio (e.g., 5 kJ/μg) and then, for energies ranging from 100 J to 1 MJ, varied the initial density and velocity over many orders of magnitude, thereby entering regions of parameter space that would be excluded by the practical considerations postulated in this paper. The approach here is to project backward from minimum ignition conditions to pick a set of initial conditions under some practical constraints. Then, time-dependent implosion calculations are conducted to determine where in initial parameter space significant fusion gain can be attained.

Findings include that ignition is possible for all three types of targets, albeit in a substantially different initial density-energy-velocity space. We show that reaching the ignition criterion does not necessarily lead to a rapid increase in temperature and high gain. The definition of initial parameters can be used to guide plasma formation research and show that initial plasmas for spherical, $B_\varphi$ cylindrical, and $B_z$ cylindrical targets must have an initial density greater than approximately $10^{17}$/cm$^3$, $10^{18}$/cm$^3$, and $10^{20}$/cm$^3$, respectively.

In Table I we list symbols that are used in this paper. The symbols are identical to those used by L&K-83 except where noted. The number of symbols listed in Table I of this paper and Table I of L&K-83 attests to the complexity of the model in spite of its simplifications.

| | | |
|---|---|---|
| Independent variable | | |
| | Time (s) | $t$ |
| Shell parameters | | |
| | Radial position (m) | $r$ |
| | Radial velocity (m/s) | $v_r$ |
| | Shell inner radius (m) | $R$ |
| | Shell outer radius (m) | $R_s$ |
| | Shell inner velocity (m/s) | $v$ |
| | Shell mass density (kg/m$^3$) | $\rho_s$ |
| | Shell inner surface area (m$^2$) | $S$ |
| | Shell kinetic energy (J) | $E$ |
| | Shell ratio of specific heats | $\gamma$ |
| Cylindrical geometry parameters | | |
| | Length (m) | $L$ |
| | Length-to-radius ratio | $L/R$ |
| | End cap area (m$^2$) | $S_E$ |
| Fuel parameters | | |
| | Fuel mass (kg) | $M$ |
| | Fuel volume (m$^3$) | $V$ |
| | Fuel mass density (kg/m$^3$) | $\rho$ |
| | Fuel ion density (/m$^3$) | $n$ |
| | End cap electron thermal conductivity (m$^{-1}$s$^{-1}$) | $K_{eE}$ |
| | Electron thermal conductivity perpendicular to Magnetic field (m$^{-1}$s$^{-1}$) | $(K_e)_\perp$ |
| | Electron thermal conductivity parallel to magnetic field (m$^{-1}$s$^{-1}$) | $(K_e)_\parallel$ |
| | Electron or ion cyclotron-frequency/collision-time product, depending upon context | $\omega\tau$ |
| | Fuel electron or ion temperature, or both, depending upon context (J) | $T$ |
| | Fuel electron temperature (J) | $T_e$ |
| | Fuel electron temperature (keV) | $T_{keV}$ |
| | Fuel ion temperature (J) | $T_i$ |
| | Fuel electron or ion pressure, or total, depending upon context (Pa) | $p$ |
| | Alpha-particle deposition fraction | $f_d$ |
| | Unmagnetized alpha deposition function | $f_\rho$ |
| | Magnetized alpha deposition function | $f_B$ |
| | Areal density (kg/m$^2$) | $\varrho R$ |
| | Areal density in cgs units (g/cm$^2$) | $(\varrho R)_c$ |
| | Axial areal density (kg/m$^2$) | $\rho L$ |

| | | |
|---|---|---|
| Magnetic field parameters | | |
| | Magnetic field, axial or azimuthal, depending upon context (T) | $B$ |
| | Axial magnetic field (T) | $B_z$ |
| | Azimuthal magnetic field (T) | $B_\varphi$ |
| | Magnetic flux (Wb) | $\Phi$ |
| | Radius-magnetic field product (T-m) | $RB$ |
| | Magnetic energy (J) | $E_b$ |
| | Current density (A/m$^2$) | $J$ |
| | Electrical resistivity (Ωm) | $\eta$ |
| | Free space permeability (C$^2$s$^2$kg$^{-1}$m$^{-3}$) | $\mu_o$ |
| | Cross-section perpendicular to B (m$^2$) | $A$ |
| | Thermoelectric heat conduction surface (m$^2$) | $S_N$ |
| | Current path length; L&K-83 used the symbol $L$ for this quantity (m) | $l$ |
| | Thermoelectric (Nernst) current path length along imploding shell (m) | $l_s$ |
| | Thermoelectric (Nernst) current path length along end caps (m) | $l_E$ |
| | Braginskii thermoelectric coefficient (1/cm$^3$) | $\beta_\wedge^{uT}$ |
| | Thermoelectric (Nernst) coefficient (1/C) | $N$ |
| | Voltage due to thermoelectric (Nernst) effect (V) | $V_N$ |
| | Voltage along perimeter: L&K-83 used $V_L$ for this quantity (V) | $V_l$ |
| Diffusion scale factors | | |
| | Radial thermal conduction scale factor | $\alpha$ |
| | Longitudinal thermal conduction scale factor | $\alpha_E$ |
| | Resistive diffusion scale factor; L&K-83 used the symbol β for this quantity | $\alpha_J$ |
| Energy interchange rates | | |
| | Electron thermal conductivity loss rate to end caps (W) | $P_{eE}$ |
| | Ion thermal conductivity loss rate to end caps (W) | $P_{iE}$ |
| | Electron radial thermal conductivity loss rate (W) | $P_{ec}$ |
| | Ion radial thermal conductivity loss rate (W) | $P_{ic}$ |
| | Electron radiation loss rate (W) | $P_{er}$ |
| | Ohmic heating rate (W) | $P_o$ |
| | Thermoelectric (Ettinghausen) conduction loss (W) | $P_{eN}$ |
| | Alpha particle redeposition rate to electrons (W) | $P_{ae}$ |
| | Alpha particle redeposition rate to ions (W) | $P_{ai}$ |
| Miscellaneous system parameters | | |
| | Ratio of plasma pressure to magnetic pressure | $\beta$ |

| | | |
|---|---|---|
| | Subscript to designate initial condition; not used if context is clear | $o$ |
| | Electronic charge or subscript to designate electron, depending upon context | $e$ |
| | Subscript to designate ion | $i$ |
| | Convergence ratio; L&K-83 used $C$ for this value | $C_R$ |

Table I. Notation. All equations use the mks system of units, shown in parentheses. Values quoted in the text and used in the figures and other tables use more conventional units.

## II. MODEL EXTENSIONS

In Table II, we introduce geometric and physical quantities for the three different geometries.

| Symbol | Description | Spherical | Cylindrical $B_\varphi$ | Cylindrical $B_z$ |
|---|---|---|---|---|
| $V$ | Fuel volume | $\frac{4\pi}{3}R^3$ | $\pi R^2 L$ | $\pi R^2 L$ |
| $S$ | Area of inner surface of shell (pusher) | $4\pi R^2$ | $2\pi RL$ | $2\pi RL$ |
| $S_E$ | End cap area | 0 | $\pi R^2$ | $\pi R^2$ |
| $A$ | Area perpendicular to magnetic field | $\frac{1}{2}\pi R^2$ | $RL$ | $\pi R^2$ |
| $S_N$ | Thermoelectric heat conduction surface | $S$ | $S + S_E$ | $S$ |
| $l$ | Current path length | $(2+\pi)R$ | $2L + \frac{4R^2}{L}$ | $2\pi R$ |
| $l_s$ | Thermoelectric current path length along imploding shell | $\pi R$ | $L$ | $2\pi R$ |
| $l_E$ | Thermoelectric current path along end caps | 0 | $2R$ | 0 |
| $K_{eE}$ | End cap electron thermal conductivity | 0 | $(K_e)_\perp$ | $(K_e)_\parallel$ |
| $\alpha_E$ | Longitudinal thermal conduction scale factor | 0 | $7/2$ | 0.2 |

Table II. New symbols related to physical extensions of the L&K-83 model. Note that L&K-83 used the symbol $L$ instead of the present $l$ for the electrical current path length. In this paper, we use $L$ as the symbol for the system length.

Following Eqs. 3 and 4 of L&K-83, for cylindrical geometry we impose a radial velocity on the shell material of the form

$$v_r = v\frac{R}{r}, \; R \leq r \leq R_s \tag{1}$$

The corresponding shell kinetic energy is

$$E = \pi\rho_s R^2 v^2 L \, ln\frac{R_S}{R} \tag{2}$$

Initially, Eq. 2 is used to determine $R_s$, and hence the volume and mass of the shell, when $E$ and $v$ are specified. Subsequently, since the energy $E$ is a dependent value (Eq. 15 of L&K-83), Eq. 2 allows the determination of $v$ from $E$ and allows for some inner surface acceleration. As with L&K-83, all time-dependent calculations reported in this paper use a shell density $\rho_s$ of 19.3 g/cm$^3$ and a shell ratio of specific heats $\gamma$ of 2.5. These two parameters together determine how much energy is required to compress the shell; lowering $\rho_s$ will increase the energy required and lowering $\gamma$ will decrease the energy. Because of the nature of the assumptions made about the shell to achieve closure—pressure equal to sum of fuel ion, electron, magnetic and radiation pressure, non-uniform but specified velocity profile, shell initially in motion with no additional energy added—there probably should be no physical significance attached to these parameters, other than the use of these values gives a reasonable estimate of efficiency and dwell times, i.e., the results are not representative of using a gold shell even though the density of gold is used. With these parameters, the simple model gives reasonable agreement with more complete results that have been published in the literature, as discussed in sections IV and VI. Presumably, the accuracy of the present model could be improved with the incorporation of a more complete shell model such as used by McBride and Slutz (reference 22).

The first modification to extend the original L&K-83 model for spherical targets to cylindrical is to include end effects. The electron energy equation, Eq. 12 of L&K-83, is modified by subtracting from the right hand side the thermal conduction to the end caps:

$$P_{eE} = S_E K_{eE} \frac{4T_e}{\alpha_E L} \tag{3}$$

where the subscript $E$ designates end, $S_E$ is the end cap surface area, $K_{eE}$ is the appropriate electron thermal conductivity indicated in Table II, $T_e$ is the electron temperature, $\alpha_E$ is a longitudinal temperature gradient scale factor indicated in Table II, and $L$ is the length of the cylinder. The factor of 4 in Eq. 3 arises because there are two end caps and the gradient is over half of the length. In Table II, $(K_e)_\perp$ and $(K_e)_\parallel$ are the electron thermal conductivity perpendicular and parallel to a magnetic field, respectively, as given by Braginskii.[23] A similar modification is made to the ion energy equation, Eq. 13, of L&K-83. For unmagnetized thermal conduction to the end caps, the scale factor $\alpha_E$ (Table II) is based upon Eq. 27 of Lindl.[24] A similar analysis for the magnetized case would lead to the value 0.25, but we use 0.2 to be consistent with L&K-83.

Equation 8 of L&K-83 defined the current density and Eq. 46 defined the voltage as

$$J = \frac{B}{\mu_o \alpha_J R};\ V_l = \eta J l \tag{4}$$

where $\alpha_J$ is a constant (Note change in notation: L&K-83 used the symbol $\beta$ instead of $\alpha_J$ and upper case $L$ instead of lower case $l$ to designate the current path length). To keep Eq. 4 valid for the cylindrical cases, we introduce the definitions of $l$ in Table II, where, for the cylindrical case with azimuthal field, the definition allows for a different scale length, but same scale factor, for the radial current at the end caps. The thermoelectric effect introduces an electron heat loss perpendicular to the current and magnetic field (i.e., Ettinghausen effect) and an electric field perpendicular to the thermal gradient and magnetic field (i.e., the Nernst effect). For the former, the loss rate is

$$P_{eN} = S_N T_e N J\ ;\ N = \frac{\beta_\wedge^{uT}}{en} \tag{5}$$

where $\beta_\wedge^{uT}$ is a Braginskii thermoelectric coefficient and e is the electronic charge. Of the several Braginskii thermoelectric coefficients, this is the only one that lends itself to a one- or zero-dimensional analysis. Eq. 5 is subtracted from the right hand side of Eq. 12 of L&K-83. For the latter, a voltage

$$V_N = N l_s \frac{T_e}{\alpha R} + N l_E \frac{2T_e}{\alpha_E L} \tag{6}$$

is generated. Eq. 10 of L&K-83 then becomes

$$\frac{d\Phi}{dt} = -V_l - V_N \tag{7}$$

and Eq. 47 of L&K-83 becomes

$$P_o = 2E_b \frac{V_l + V_N}{\Phi} \tag{8}$$

Eq. 8 includes the heating that corresponds to Eqs. 6 and 7.

The alpha particle deposition of L&K-83 Eq. 41 as used in this paper is given by

$$f_d = \frac{1}{1+\frac{1}{f_\rho + f_B}} \tag{9}$$

where

$$f_\rho = 0.526 * (\varrho R)_c\left(1 + 122 * T_{keV}^{-1.25}\right) \qquad (10)$$

and

$$f_B = 0.0843 * \left(\frac{RB}{0.2703}\right)^2 \qquad (11)$$

In Eq. 10, $(\varrho R)_c$ is the areal density in cgs units (g/cm$^2$) and $T_{keV}$ is the temperature in units of keV. In Eq. 11, $RB$ is the radius-magnetic field product in units of MG-cm. The form of Eqs. 9-11 is chosen for convenience in reprogramming the Fortran of the original L&K-83 computer code.

When either $f_\rho$ or $f_B$ are large, $f_d$ approaches unity. Note that the quantity in parentheses in Eq. 11 is the ratio of the radius to the alpha particle Larmor orbit. When $RB$ is zero, $f_d$ has the form given by Duderstadt and Moses.[25] When $(\varrho R)_c$ is small, which is the main interest in this article, $f_d$ approximates within several percent the value given by Basko.[26] Although the deposition determined by Basko was in an open-field-line geometry, Basko notes "we expect that in the case of spherical targets, once a magnetic field is created which is parallel to the surface of a DT sphere, the MTF ignition criterion should be very similar to the cylindrical case analyzed here." However, Basko also notes "an interesting alternative to the quasi-uniform axial magnetization would be a cylinder with an azimuthal (phi) magnetic field. However, a detailed analysis of such a configuration in the context of MTF should involve more complex electrodynamics of the whole target and remains for future work. Note that the phi field must vanish on the cylinder axis, i.e., exactly where one expects an igniting hot core of magnetized fuel to be formed." Although these concerns are certainly valid, nevertheless, to get at least an initial insight into the parameter space in which cylindrical and spherical targets with an azimuthal field might operate, we use Eq. 9 for all three geometries considered under the presumption that Eq. 9 will apply approximately when the system radius is significantly larger than the average alpha particle Larmor orbit.

Analogous with Slutz-10, we define the ignition criterion (or condition) as the point where the thermonuclear energy deposition rate equals the sum of radiation and conduction loss rates, i.e., when

$$P_{\mathrm{ae}} + P_{\mathrm{ai}} = P_{\mathrm{ec}} + P_{\mathrm{ic}} + P_{\mathrm{er}} + P_{eN} + P_{\mathrm{eE}} + P_{\mathrm{iE}} \qquad (12)$$

where $P_{\mathrm{ae}}$ and $P_{\mathrm{ai}}$ are the rate of alpha particle energy deposited in the electrons and ions, respectively, as defined in L&K-83 Eq. 41, $P_{\mathrm{ec}}$ and $P_{\mathrm{ic}}$ are the electron and ion thermal conduction losses to the imploding shell as defined in L&K-83 Eqs. 34 and 35, $P_{\mathrm{er}}$ is the electron radiation loss as defined in L&K-83 Eq. 37, $P_{\mathrm{eE}}$ and $P_{\mathrm{iE}}$ are defined by Eq. 3 above and its ion equivalent, and $P_{eN}$ is the thermoelectric effect as defined in Eq. 5. $P_{eN}$ is not considered in the usual ignition analyses; furthermore, most analyses set the thermal conduction scale factors, $\alpha$ and $\alpha_{E,}$ to unity. For completeness, Ohmic heating should also be included in Eq. 12, although we will ignore it since it is expected to be small at ignition temperatures. The interest in ignition, of course, stems from the fact that the fusion reaction rate increases rapidly with temperature, so once the energy deposition exceeds the losses, the temperature and the fusion rate potentially increase rapidly, leading to a large fractional fuel burn-up.

Ignition is absolutely required in conventional ICF targets. Whether or not ignition is necessary in MTF remains a research topic. As L&K-83 showed, magnetized targets can have significant fuel burn-up and useful energy gain even without fuel self heating. However, as discussed later, fuel self-heating may actually occur in the parameter space considered by L&K-83, decreasing the gain by reducing convergence.

A useful magnetized target implosion is a quasi-adiabatic, quasi-flux-conserving process. To the extent that the process is adiabatic and flux conserving, physical values of interest at any radial convergence ratio $C_R$=$R_o/R$ can be related to the initial conditions as tabulated in Table III.

| | $n/n_o$ | $\rho/\rho_o$ | $T/T_o$ | $B/B_o$ | $(\omega\tau)^2/(\omega\tau)_o^2$ | $p/p_o$ | $\beta/\beta_o$ |
|---|---|---|---|---|---|---|---|
| Cylindrical $B_z$ | $C_R^2$ | $C_R^2$ | $C_R^{4/3}$ | $C_R^2$ | $C_R^4$ | $C_R^{10/3}$ | $C_R^{-2/3}$ |
| Cylindrical $B_\varphi$ | $C_R^2$ | $C_R^2$ | $C_R^{4/3}$ | $C_R$ | $C_R^2$ | $C_R^{10/3}$ | $C_R^{4/3}$ |
| Spherical $B_\varphi$ | $C_R^3$ | $C_R^3$ | $C_R^2$ | $C_R^2$ | $C_R^4$ | $C_R^5$ | $C_R$ |

Table III. Dependence of various physical quantities on the convergence ratio $C_R$=$R_o/R$ if the implosion process is adiabatic and magnetic flux conserving.

By definition, the time-dependent computations with the model as reported in this paper satisfy the density $n$ ($\rho$) relationship in Table III. However, the temperature $T$ and the magnetic field $B$, and hence the remaining quantities, do not necessarily satisfy the relationships in Table III, depending upon thermal and magnetic flux losses or thermal energy gain due to alpha particle deposition.

In the sections III-VI, we will consider several cases of each type of target. To distinguish one type of target from another, cylindrical $B_Z$ case numbers will be prefixed with a Z, cylindrical $B_\phi$ case numbers will be prefixed with a Φ, and spherical case numbers will be prefixed with an S.

## III. CYLINDRICAL TARGETS WITH AXIAL MAGNETIC FIELD ($B_z$)

Cylindrical targets using an axial magnetic field reduce heat losses only in the radial direction and are subject to unmagnetized heat conduction in the axial direction. Therefore it is anticipated that the length of the target at ignition will have to be significantly longer than the radius. Therefore, as an example, we will consider the ratio of length-to-radius ($L/R$) of 50. Fig. 1 shows the minimum size (Fig. 1-left) for ignition in targets with an ignition $\beta$, the ratio of fuel pressure to magnetic pressure at ignition, equal to unity, and the corresponding $RB$ product (Fig. 1-right) with $L/R$=50.

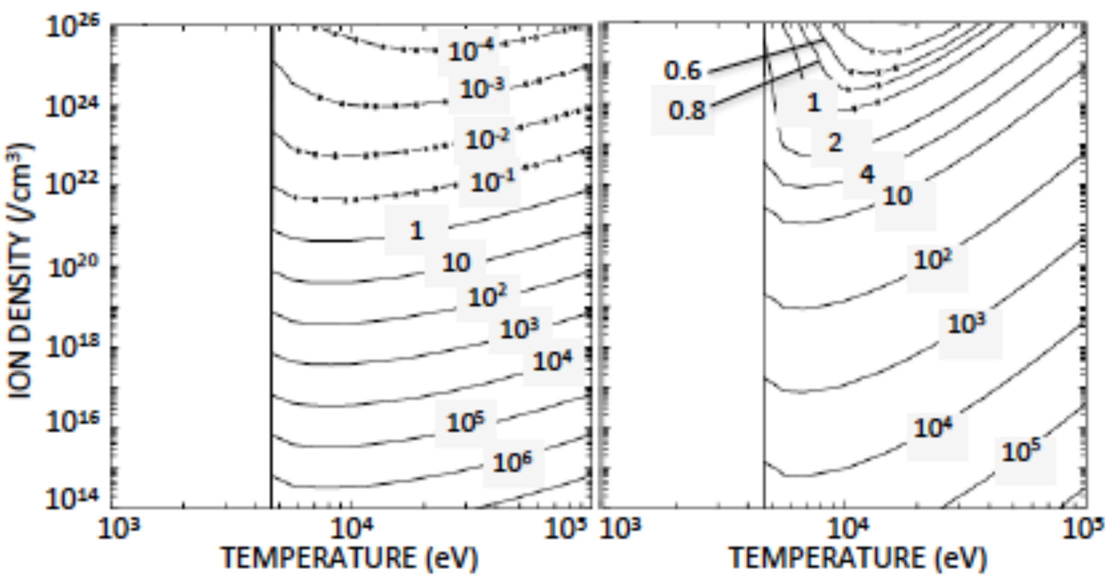


Fig. 1. The minimum radius (left; units-cm) and $RB$ product (right; units—MG-cm) for ignition in cylindrical targets with an axial ($B_z$) magnetic field ($L/R$=50, $\beta$=1).

At a given density, the minimum size for ignition generally occurs at a temperature of 6-8 keV. Fig. 2 shows how the minimum size, minimum fuel energy (sum of plasma and magnetic), and corresponding magnetic field vary with density for different values of ignition $\beta$ at 7 keV. At densities lower than about $10^{21}/\text{cm}^3$, the minimum size and energy are essentially independent of $\beta$. This is because the radial thermal conduction becomes essentially negligible and the product $RB$ is large enough for 100% alpha particle deposition (Eq. 11). Therefore, the system length is determined by axial thermal conduction and the radius is 1/50 of the length, hence the extremely high $RB$ at low densities (Fig. 1 right; as shown in sections V and VI, the other types of targets do not have such high $RB$ at low density). The $\rho L$ required is around 0.08-0.2 g/cm$^2$, which is somewhat less than the $\rho R$ of 0.4 g/cm$^2$ of conventional, unmagnetized targets, due to the negligible radial conduction and 100% deposition. Note that Eqs. 9 and 11 do not take into account the effect of length on alpha deposition, under the assumption that the length is much longer than many Larmor orbits (the treatment of the relatively small fraction of alpha particles born with axial, or near axial, velocity is beyond the scope of this paper).

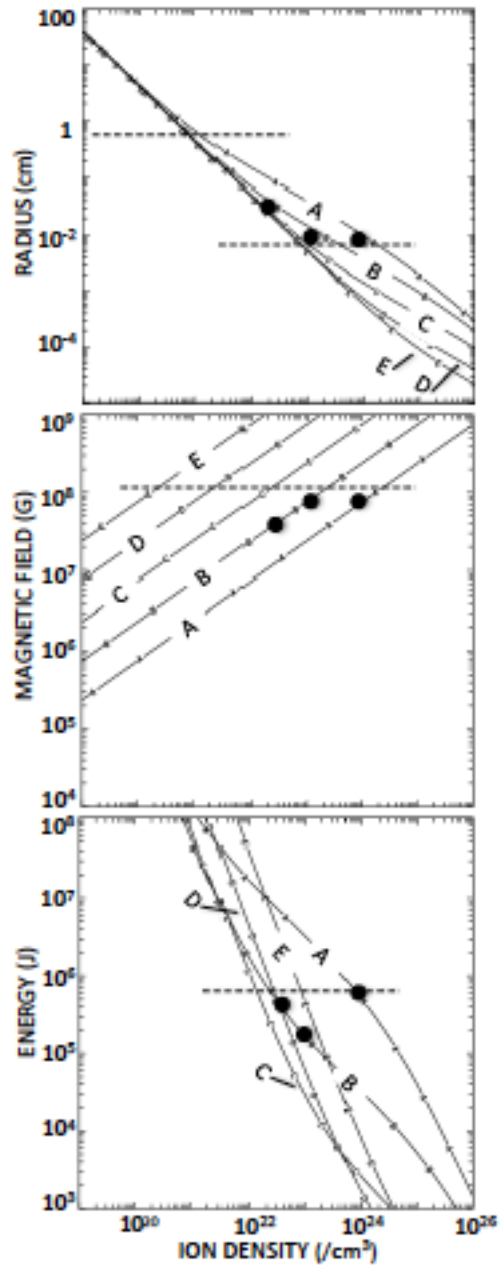


Fig. 2. The minimum radius (top), corresponding magnetic field (middle) and required sum of fuel thermal and magnetic energy (bottom) for ignition at 7 keV as a function of ion density for $\beta$ at ignition equal to 100 (A), 10 (B), 1 (C), 0.1 (D), and 0.01 (E) for cylindrical targets with an axial ($B_z$) magnetic field ($L/R$=50). The dotted lines show the approximate practical limits on size, energy, and magnetic field as discussed in the text. The solid dots indicate cases Z.1, 2 and 3 considered in the text.

One clear advantage of magnetized targets is the possibility of reaching significant fusion burn at a radial convergence ratio $C_R$ significantly less than the $C_R$ of 35-40 required with conventional unmagnetized targets. Therefore, we will assume that the final $C_R$ must be limited to 20-30. Figures 1 and 2 show the minimum conditions at ignition required to satisfy the ignition criterion (Eq. 12). Since these are equilibrium conditions at which fusion energy deposition rate equals the total loss rate, it is to be expected that true ignition and burn where the ion temperature rapidly increases and significant energy gain is obtained will only occur when the density, temperature, and magnetic field are larger than the minimum conditions. Therefore, we will postulate that the ignition conditions must be reached at approximately a $C_R$=15 to limit the maximum $C_R$ to 20-30.

Fig. 2 and some practical limits allow us to place some approximate bounds on the parameter space in which cylindrical $B_z$ targets can operate. We postulate that the practical initial size (radius) of a target should be between, say, 0.1-10 cm, which implies that the compressed radius at a $C_R$=15 must lie between 0.0067 cm and 0.67 cm. Secondly, we will postulate that it is not likely that any existing and near term driver can couple more than 0.5 MJ of thermal and magnetic energy to the fusion fuel at ignition; in general, to couple as much as 0.5 MJ to the fuel, a multi-megajoule driver would be required. Furthermore, based on the MagLIF work, we will postulate that an initial magnetic field is limited to approximately 500 kG. To the extent that the compression process is flux-conserving, Table III then implies that the magnetic field at a $C_R$ of 15 will be less than 113 MG.

The dotted lines in Fig. 2 show the postulated limits of size, energy, and magnetic field at ignition. Under the dimensional limits, Fig. 2-top shows that the $B_z$ targets must operate in the density range of approximately $10^{21}$-$10^{24}$/cm$^3$. From Fig. 2-bottom, the energy limit constrains the density at ignition to be greater than $10^{22}$/cm$^3$. And from Fig. 2-middle, the magnetic field limit constrains the density to be lower than $2\text{x}10^{24}$/cm$^3$. Overall, these conditions mean that the ignition $\beta$ must be greater than 1 and the density must be between approximately $10^{22}$/cm$^3$ (0.042 g/cm$^3$) and $10^{24}$/cm$^3$ (4.2 g/cm$^3$), depending upon $\beta$. The impact of the practical limits is summarized in table IV.

Clearly, it could be argued that our postulated limits are not restrictive enough. The analysis leading to Table IV can readily be repeated for other limit choices either more restrictive or less restrictive than used in this paper. For example, an increase in energy lowers the lower bound on density.

| Condition\β | 0.01 | 0.1 | 1 | 10 | 100 |
|---|---|---|---|---|---|
| Size | $10^{21}$-5x$10^{22}$ | $10^{21}$-5x$10^{22}$ | $10^{21}$-8x$10^{22}$ | $10^{21}$-3x$10^{23}$ | 2x$10^{21}$-$10^{24}$ |
| Energy | >$10^{23}$ | >3x$10^{22}$ | >2x$10^{22}$ | >3x$10^{22}$ | >$10^{24}$ |
| Magnetic field | <2x$10^{20}$ | <2x$10^{21}$ | <2x$10^{22}$ | <2x$10^{23}$ | <2x$10^{24}$ |
| Overall | ---- | ---- | --- | 3x$10^{22}$-2x$10^{23}$ | 1-2x$10^{24}$ |

Table IV. Approximate compressed density range (/cm$^3$) for cylindrical targets with axial magnetic field ($B_z$) and ignition at 7 keV based upon compressed size in the range 0.0067-0.67 cm, the sum of the compressed magnetic and thermal energy less than 500 kJ, and compressed magnetic field less than 113 MG ($L/R$=50).

Within the practical limits, $B_z$ targets have a potential operating range covering two orders of magnitude in density, showing a clear advantage of magnetized targets over conventional targets that have a much more limited density range. Furthermore, the $\rho R$ required is far below the 0.4 g/cm$^2$ of conventional targets, e.g., at $10^{23}$/cm$^3$, 7 keV, $\beta$=10 and $L/R$=50, the $\rho R$ is 0.003 g/cm$^2$. Even at $10^{24}$/cm$^3$, 7 keV, $\beta$=100, and $L/R$=50, the $\rho R$ is only approximately 0.04 g/cm$^2$. Of course, the reduction in $\rho R$ is due to the thermal conduction reduction and alpha deposition enhancement by the magnetic field. Fig. 2 implies the $RB$ product in the useful density range must be of the order of 1 MG-cm, i.e., the system radius must be approximately 4 times larger than the alpha particle Larmor orbit. In this parameter range, radiation losses are 0.3-1 times the conduction losses.

The energy required depends upon the length. If the compressed $L/R$=50 at $C_R$=15, then the initial $L/R$=3.3, so practical considerations may preclude much shorter length. Table V shows an example of the effect of the $L/R$ ratio. For the $n$-$T$-$B$ combination chosen, there is actually a minimum in the energy required at $L/R$=35, with the energy required increasing with both increasing and decreasing $L/R$ ratio. On the other hand, the energy per unit length and the radius decrease as the length is increased, asymptotically approaching the energy per unit length and radius that would be required if axial losses were negligible.

| $L/R$ | $R$(cm) | $L$(cm) | $E_{ig}$ (kJ) | $E_{ig}/L$ (kJ/cm) |
|---|---|---|---|---|
| 10 | 0.0293 | 0.29 | 282 | 972 |
| 20 | 0.0190 | 0.38 | 154 | 405 |
| 35 | 0.0154 | 0.54 | 144 | 266 |
| 50 | 0.0143 | 0.71 | 165 | 232 |
| 75 | 0.0136 | 1.02 | 214 | 210 |
| 100 | 0.0133 | 1.34 | 270 | 201 |

Table V. Dependence of ignition size and energy required on $L/R$ ratio for $n$=$10^{23}$/cm$^3$, $T$=7 keV, $B_z$=75.1 MG ($\beta$=10).

To the extent that the implosion process is adiabatic and flux conserving, the relationships in Table III allow the determination of the initial conditions required to meet the minimum ignition conditions at a desired compression ratio $C_R$. As examples, we will consider three cases shown in Table VI; these cases are shown as dots on Fig. 2. These cases meet the practical conditions on size, magnetic field, and energy.

| | Ignition conditions | | | | | | | | Initial conditions | | | | |
|---|---|---|---|---|---|---|---|---|---|---|---|---|---|
| Case | $n$ | $B_z$ | $R$ | $L$ | $RB$ | $M$ | $E_{ig}$ | $\beta$ | $n$ | $\rho$ | $B_z$ | $R$ | $\beta$ |
| Z.1 | 3x10$^{22}$ | 41.1 | 0.030 | 1.52 | 1.23 | 0.55 | 479 | 10 | 1.33x10$^{20}$ | 0.55 | 0.18 | 0.457 | 60.8 |
| Z.2 | 10$^{23}$ | 75.1 | 0.014 | 0.71 | 1.05 | 0.19 | 165 | 10 | 4.45x10$^{20}$ | 1.86 | 0.33 | 0.214 | 60.8 |
| Z.3 | 10$^{24}$ | 75.1 | 0.0098 | 0.49 | 0.74 | 0.61 | 500 | 100 | 4.45x10$^{21}$ | 18.6 | 0.33 | 0.147 | 608 |

Table VI. Ignition condition examples at 7 keV and corresponding initial conditions for cylindrical targets with axial magnetic field ($B_z$) under the assumptions of adiabaticity and flux conservation ($C_R$=15, compressed $L/R$=50). The ignition energy $E_{ig}$ is the sum of fuel thermal and magnetic energies. The corresponding initial temperature is 189 eV. Units: $n$—/cm$^3$; $\rho$—mg/cm$^3$; $B_z$—MG; $RB$—MG-cm; $R$, $L$—cm; fuel mass $M$—mg; $E_{ig}$—kJ.

The extent to which an MTF implosion is adiabatic and flux conserving, the degree to which the ignition conditions can be reached, and the energy gain that can be achieved can only be determined by detailed time-dependent implosion calculations. That is the purpose of the simple implosion model discussed in this paper, where in addition to the initial conditions on density, magnetic field, and radius (e.g., Table VI), the initial temperature, velocity and kinetic energy must be specified. As L&S-09 show, the minimum required implosion velocity at any *n-T-B-R* combination can be estimated by setting the energy loss rate to the compressional work rate (L&S-09 Eq. 17). However, in practice, the required velocity at any *n-T-B-R* combination is significantly higher than L&S-09 Eq. 17 would estimate, since the estimated velocity is that required simply to maintain an equilibrium, not to increase the temperature. Clearly, the initial kinetic energy must be sufficient to provide the thermal and magnetic energy at ignition as well as overcome energy losses during the implosion and providing the energy required to compress the pusher.

Although L&S-09 Eq. 17 would allow a lower velocity bound to be estimated for a given *n-T-B-R* combination, an implosion history passes through many *n-T-B-R* combinations so L&S-09 Eq. 17 has limited use in determining an actual initial velocity. The optimum velocity and corresponding energy can only be determined by essentially trial-and-error by performing many time-dependent implosion calculations. For the sets of initial *n-B-R* values in table VI, a series of computations was performed to determine the values of initial velocity and kinetic energy that approximately optimize the gain. In our first computations using an initial temperature of 189.2 eV, i.e., the temperature required to reach 7 keV at $C_R$=15 if the process were adiabatic, we found that the implosion process was quite non-adiabatic with the temperature increasing approximately as $C_R^{1.1\text{-}1.2}$, rather than as $C_R^{4/3}$ as given in Table III, and the implosions reached a $C_R$ greater than 30. Therefore, the initial temperature was increased to 250 eV.

Table VII summarizes the computational results. All cases gave gains greater than 15, where the gain is the ratio of the fusion energy produced divided by the initial kinetic energy. Fig. 3 shows how the ion temperature varied with convergence ratio during the compression and subsequent expansion. Because the implosion process was non-adiabatic, as Fig. 3 shows, ignition occurred at a $C_R$ greater than the targeted 15 and a higher *RB* (for cases Z.1 and Z.2). After the ignition condition is reached, both hydrodynamic heating due to compression by the shell and self-heating due to alpha particle deposition contribute to the subsequent increase in temperature. Fig. 3 also shows a rapid increase in ion temperature with peak temperature being reached after maximum compression and after the imploding shell has begun to rebound. The rapid increase starts at a $C_R$ higher than that at which the ignition condition is reached.

A few general statements can be made about these computations. As the maximum magnetic field shows, 14-20% of the magnetic flux is lost during the implosion. A similar fraction is lost during the subsequent expansion. The thermoelectric (i.e., Nernst) effect is responsible for 70-100% of this loss. At the beginning of the implosion, radiation losses are 10-25% of the thermal conduction losses for Z.1 and Z.2, and approximately 80% for Z.3, and become comparable to or slightly exceed the conduction losses at peak compression. For Z.1 and Z.2, end losses are about 10% of the total conduction losses at the start, decrease early in the implosion, then increase to be about 90% of the total conduction losses at peak compression. For Z.3, the end losses are initially about 2% and increase to about 30% of the total. For all cases, the heat loss due to the thermoelectric (i.e., Ettinghausen) effect is approximately 1% of the total.

| Case | Initial | | At ignition | | | | | Maximum | | | | |
|---|---|---|---|---|---|---|---|---|---|---|---|---|
| | $v$ | $E$ | $n$ | $B_z$ | $RB$ | $T_i$ | $C_R$ | $n$ | $B_z$ | $T_i$ | $C_R$ | Gain |
| Z.1 | 4 | 1 | $6.04\times10^{22}$ | 68.9 | 1.48 | 5.85 | 21.3 | $1.05\times10^{23}$ | 120 | 27.1 | 28.1 | 19.3 |
| Z.2 | 7.5 | 0.67 | $1.38\times10^{23}$ | 88.9 | 1.08 | 6.66 | 17.6 | $3.78\times10^{23}$ | 244 | 52.7 | 29.2 | 16.4 |
| Z.3 | 15 | 3 | $1.55\times10^{24}$ | 92.2 | 0.73 | 7.11 | 18.6 | $2.59\times10^{24}$ | 153 | 51.7 | 24.2 | 27.0 |

Table VII. Initial velocity $v$ and initial kinetic energy $E$ that approximately maximize gain for the initial $n$, $B_z$, and $R$ specified in table VI and an initial temperature $T$=250 eV. Also shown are subsequent conditions at ignition, i.e., when fusion energy deposition rate equals total loss rate. Also shown are the maximum values reached in the computations. Units: $v$—cm/μs; $E$—MJ; $n$—/cm$^3$; $B_z$—MG; $RB$—Mg-cm; $T_i$—keV.

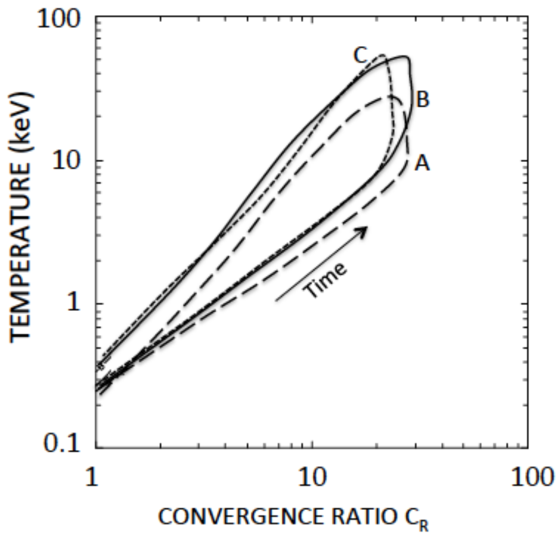


Fig. 3. The ion temperature evolution for cases Z.1 (A), Z.2 (B), and Z.3 (C). Time increases counterclockwise from the initial temperature value of 250 eV.

Additional computations for the parameters of case Z.2 showed that an increase in initial density from 4.45 x $10^{20}/cm^3$ to 7.5 x $10^{20}/cm^3$ increased the gain from 16.4 to 31.5 and reduced the convergence to 24.6. Fig. 4 shows how the gain and convergence vary with other initial parameters at the higher density. Fig. 4 shows that useful gain can be obtained at potentially achievable convergences over a wide variation in initial conditions, showing that magnetized targets are not as sensitive to system parameters as are conventional targets.

Fig. 4 shows characteristics that are more-or-less common to all three types of targets. Fig. 4A--there is a density for which the gain is a maximum when all other parameters are held fixed. At a higher density, the temperature increases more slowly due to increased losses and therefore ignition is not achieved. At a lower density, the fusion reaction rate is reduced, reducing the gain. Fig. 4B--for the same initial conditions for the other variables, the gain decreases for a larger magnetic field because both the plasma pressure and the magnetic back pressure increase, reducing the convergence. On the other hand, below about 200 kG, the magnetic reduction of thermal conductivity is insufficient to allow heating to ignition temperatures. Fig. 4C--the gain can be further increased by a reduction in initial temperature, albeit with an increase in convergence. Fig. 4D--there is a minimum velocity below which the shell hydrodynamic work rate is low enough that the temperature does not increase sufficiently to achieve ignition, and fuel pressure does not build up sufficiently to limit the convergence. For example, at 5 cm/μs, the temperature increases slower than than $C_R^{1.05}$ and only reaches a temperature of 4.7 keV when the implosion terminates at $C_R$=24.4 due to magnetic back-pressure. Fig. 4E--with increased energy, the yield increases but the gain goes down. At lower energies, the compression does not reach a value large enough to achieve ignition.

This example illustrates the complex, nonlinear behavior retained even in the simple implosion model.

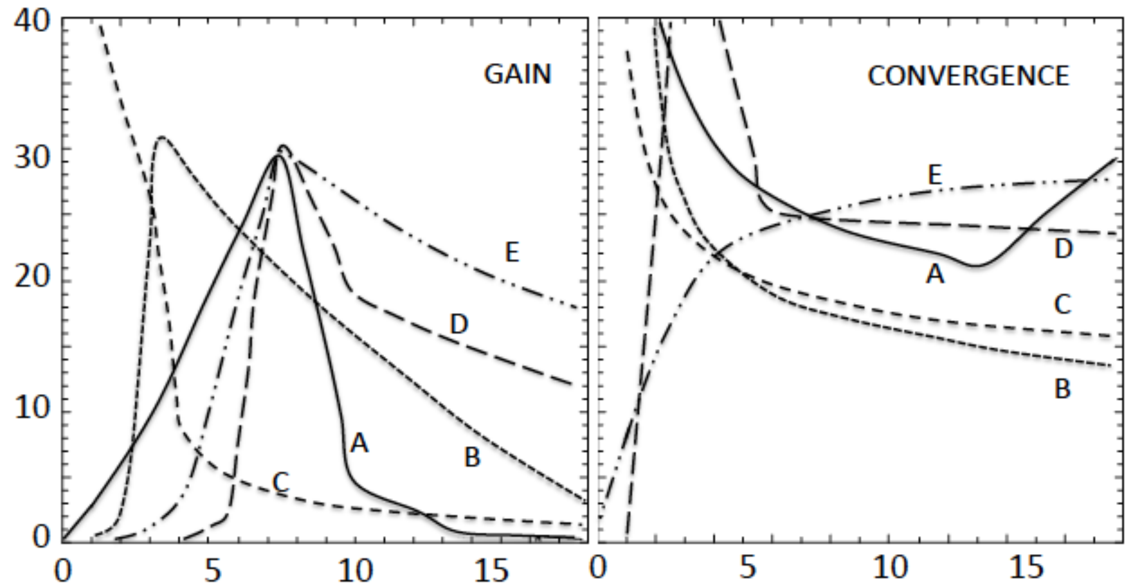


Fig. 4. The variation of gain (left) and convergence ratio (right) with variation in initial parameters for a basic cylindrical target parameter set of $n$=7.5 x $10^{20}$/cm$^3$, $T$=250 eV, $B_z$=334 kG, $R$=0.214 cm, $L$=0.71 cm, $v$=7.5 cm/μs, $E$=670 kJ (case Z.2 at higher density).

One of the potential tradeoffs in MTF is initial temperature vs. convergence ratio. As Table III implies, an increase in initial temperature can reduce the convergence required to reach fusion temperatures. Fig. 4C shows this effect, albeit with the gain decreasing as the convergence is decreased. It is reasonable to ask whether or not gains comparable to those in Table VII can be achieved at significantly lower convergence. The initial conditions for the cases considered so far were based upon ignition conditions being reached at $C_R$ =15 if adiabatic and flux conserving. If, for example, $C_R$=10 is considered, our practical considerations change the range of compressed radius to 0.01-1 cm and reduce the compressed magnetic field to 50 MG. The size limitations raise the dotted lines of Fig. 2-top by a factor of 1.5 and the reduced magnetic field limitation lowers the dotted line of Fig. 2-middle by a factor of 2.25. An examination of Fig. 2 shows that these limitations substantially decrease the range of density and $\beta$ that meet all of the practical limitations on size, field, and energy.

Table VIII-top shows three cases covering the narrow density range that can be accessed with a targeted $C_R$=10. All three cases have an initial magnetic field and an ignition energy just below the postulated limits. For all three cases, a relatively small decrease in $\beta$ reduces the magnetic field but increases the ignition energy above the limit. Similarly, a relatively small increase in $\beta$ reduces the ignition energy but increases the initial magnetic field above the limit. For example, the operating $\beta$ range for $n$=2 x $10^{22}$/cm$^3$ is approximately 4-6. Table VIII-bottom shows the corresponding calculations using a velocity and energy that approximately maximize the gain. As in the previous cases, the temperature increases slower than adiabatic so the calculations used an initial temperature of 400 eV instead of the 325 eV that would be appropriate for an adiabatic compression. All three cases of table VIII reach ignition at $C_R$ less than or equal to 13 and all reach high gain at a $C_R$ less than 20. The dependency on initial parameters for all three cases is qualitatively similar to Fig. 4. For each case an increase in initial density leads to an increased gain at a reduced convergence, e.g., increasing the initial density for case Z.5 to 7.5 x $10^{20}$/cm$^3$ increases the gain to 30 and reduces the convergence to 16.6 and increasing the initial density for case Z.6 to 1.3 x $10^{21}$/cm$^3$ increases the gain to 32.8 and decreases the convergence to 16.3.

| | Ignition conditions | | | | | | | | Initial conditions | | | | |
|---|---|---|---|---|---|---|---|---|---|---|---|---|---|
| Case | $n$ | $B_z$ | $R$ | $L$ | $RB$ | $M$ | $E_{ig}$ | $\beta$ | $n$ | $\rho$ | $B_z$ | $R$ | $\beta$ |
| Z.4 | 2x$10^{22}$ | 47.5 | 0.034 | 1.68 | 1.59 | 0.49 | 453 | 5 | 2x$10^{20}$ | 0.83 | 0.475 | 0.336 | 23.2 |
| Z.5 | 5x$10^{22}$ | 44.4 | 0.025 | 1.26 | 1.11 | 0.52 | 437 | 14.3 | 5x$10^{20}$ | 2.07 | 0.444 | 0.250 | 66.3 |
| Z.6 | $10^{23}$ | 48.8 | 0.021 | 1.01 | 1.01 | 0.58 | 483 | 23.7 | $10^{21}$ | 4.15 | 0.488 | 0.207 | 110 |

| | Initial | | At ignition | | | | | Maximum | | | | |
|---|---|---|---|---|---|---|---|---|---|---|---|---|
| Case | $v$ | $E$ | $n$ | $B_z$ | $RB$ | $T_i$ | $C_R$ | $n$ | $B_z$ | $T_i$ | $C_R$ | Gain |
| Z.4 | 3.5 | 2 | 2.82x$10^{22}$ | 63.4 | 1.79 | 6.37 | 11.9 | 6.39x$10^{22}$ | 143 | 40.8 | 17.9 | 12.2 |
| Z.5 | 5 | 2 | 8.20x$10^{22}$ | 64.2 | 1.26 | 6.17 | 12.8 | 1.69x$10^{23}$ | 132 | 52.1 | 18.4 | 18.5 |
| Z.6 | 7 | 2 | 1.70x$10^{23}$ | 71.7 | 1.14 | 6.68 | 13.0 | 3.13x$10^{23}$ | 131 | 56.1 | 17.7 | 22.9 |

Table VIII. Targeted ignition conditions and corresponding initial conditions ($C_R$ = 10; compressed $L/R$=50; top) and computed initial, ignition, and maximum conditions (bottom) for high-gain, low convergence cylindrical targets with axial magnetic field ($B_z$) and an initial temperature of 400 eV. Units: $n$—/cm$^3$; ρ—g/cm$^3$; $B_z$—MG; $T$--keV; $R,L$—cm; $RB$—Mg-cm; $v$—cm/us; fuel mass $M$—mg; $E$—MJ.

For all examples considered in this section, the initial plasmas are very high $\beta$, with the initial $\beta$ ranging from 20 to over 600 and the initial density ranging from $10^{20}$/cm$^3$ to 5 x $10^{21}$/cm$^3$. The formation of magnetized plasmas in this $\beta$-$n$ range at the 250 eV-400 eV initial temperature considered represents a formidable challenge and would appear to be a greater challenge than driver development, where the requisite velocities (3.5-15 cm/μs), implosion kinetic energies (0.6-3 MJ) and convergences are in or near the range that have already been attained experimentally with magnetically driven liners, one type of candidate MTF driver.

## IV. A COMPARISON WITH MAGLIF SIMULATIONS

Slutz-10 and S&V-12 have reported one-dimensional simulations of cylindrical $B_z$ targets that could potentially be imploded with the existing Z machine or subsequent upgrades. These simulations include much more physics than the simple model reported in this paper, including realistic liner implosion drive conditions (as opposed to the system being set initially in motion as in our model), realistic representation of the imploding pusher material properties, and the development of non-uniform profiles within the fuel.

To model the same situations as Slutz-10 and S&V-12, we have used initial dimensions, density, temperature and magnetic field approximately equal to those reported by those authors. To get a representative velocity and kinetic energy, we have conducted some simple zero-dimensional implosion calculations using the Z current waveforms reported by the authors. The complete initial conditions for our computations are shown in Table IX. Note that these conditions would be projected to reach 7 keV at a $C_R$ of approximately 13. For the projected conditions at a length of 0.5 cm, the minimum mass for ignition would be 0.35 mg and 0.65 mg, slightly higher than the actual masses used; since, of course, some hydrodynamic heating is provided by the imploding pusher as the ignition condition is approached, this slight mass difference does not necessarily preclude ignition.

| | Initial conditions | | | | | | | | | Projected at 7 keV | | | | |
|---|---|---|---|---|---|---|---|---|---|---|---|---|---|---|
| Case | $n$ | $\rho$ | $B_z$ | $T$ | $R$ | $M$ | $v$ | $E$ | $\beta$ | $C_R$ | $n$ | $B_z$ | $RB$ | $\beta$ |
| Z.7 | $7.22\times10^{20}$ | 3 | 0.3 | 0.225 | 0.27 | 0.34 | 5 | 0.55 | 146 | 13.2 | $1.25\times10^{23}$ | 52.1 | 1.07 | 25 |
| Z.8 | $1.52\times10^{21}$ | 6.3 | 0.3 | 0.250 | 0.25 | 0.62 | 10 | 1.5 | 340 | 12.2 | $2.25\times10^{23}$ | 44.4 | 0.91 | 63 |

Table IX. Initial conditions for computations comparable to Slutz-10 (Z.7) and S&V-12 (Z.8). The length for both cases is 0.5 cm. Also shown are the projected conditions when the temperature reaches 7 keV, based upon adiabaticity and flux conservation. Units: $n$—/cm$^3$; $\rho$—mg/cm$^3$; $B_z$—MG; $RB$—MG-cm; $T$—keV; $R$—cm; fuel mass $M$—mg; $v$—cm/μs; $E$—MJ.

Fig. 5 shows the temperature history of the two computations. Whereas case Z.7 (Fig. 5A) did not ignite, case Z.8(Fig. 5B) ignited and shows the characteristic rapid temperature increase, reaching a peak temperature of 71 keV. In case Z.7, the maximum energy deposition rate was 95% of the loss rate, whereas, in case Z.8, the peak deposition rate was 8.2 times larger than the loss rate at the same time.

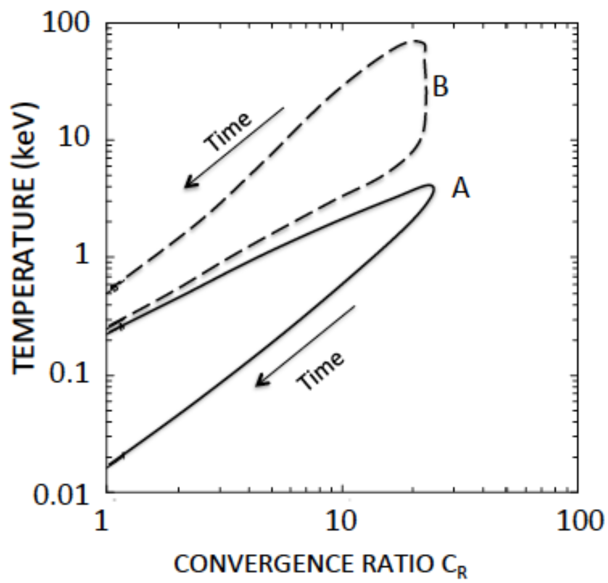


Fig. 5. Temperature history for case Z.7 (A) and Z.8 (B).

Computed results are summarized in Table X for the full physical model and selected subsets. Since the MagLIF simulations were one-dimensional and did not include end losses, cases Z.7a and Z.8a correspond most closely to those previously reported by Slutz-10 and S&V-12. In spite of the fundamental differences in the two approaches, our model results have features of the more complete results. Slutz-10 reported a convergence of 25 that is comparable to the 24.7 of Z.7a, a final field of 130 MG comparable to the Z.7a maximum of 137 MG, and a yield of 500 kJ comparable to Z.7a 516 kJ.

| Case | At ignition | | | | | Maximum | | | | | | |
|---|---|---|---|---|---|---|---|---|---|---|---|---|
| | $n$ | $B_z$ | $T_i$ | $C_R$ | $RB$ | $n$ | $B_z$ | $T_i$ | $C_R$ | $RB$ | Yield | Gain |
| Z.7 | ---- | ---- | ---- | ---- | ---- | 4.70x10$^{23}$ | 147 | 4.09 | 24.4 | 1.56 | 0.449 | 0.8 |
| Z.7a | ---- | ---- | ---- | ---- | ---- | 4.40x10$^{23}$ | 137 | 4.27 | 24.7 | 1.50 | 0.516 | 0.92 |
| Z.7b | ---- | ---- | ---- | ---- | ---- | 3.51x10$^{23}$ | 143 | 5.21 | 22.0 | 1.76 | 0.891 | 1.59 |
| Z.7c | ---- | ---- | ---- | ---- | ---- | 9.56x10$^{23}$ | 269 | 3.79 | 36.4 | 2.00 | 0.308 | 0.55 |
| Z.7d | ---- | ---- | ---- | ---- | ---- | 9.71x10$^{23}$ | 273 | 3.66 | 36.6 | 2.01 | 0.260 | 0.47 |
| Z.7e | ---- | ---- | ---- | ---- | ---- | 1.85x10$^{24}$ | ---- | 1.64 | 50 | ---- | 0.008 | 0.015 |
| Z.8 | 4.38x10$^{23}$ | 72.1 | 5.84 | 17.0 | 1.06 | 8.14x10$^{23}$ | 133 | 70.8 | 23.2 | 1.44 | 63.2 | 41.5 |
| Z.8a | 4.42x10$^{23}$ | 72.7 | 6.06 | 17.1 | 1.06 | 7.91x10$^{23}$ | 129 | 81.7 | 22.8 | 1.42 | 65.5 | 43.1 |
| Z.8b | 3.65x10$^{23}$ | 71.7 | 5.73 | 15.5 | 1.16 | 7.11x10$^{23}$ | 140 | 89.0 | 21.6 | 1.62 | 63.4 | 41.7 |
| Z.8c | ---- | ---- | ---- | ---- | ---- | 1.13x10$^{24}$ | 184 | 9.13 | 27.3 | 1.69 | 11.8 | 7.77 |
| Z.8d | ---- | ---- | ---- | ---- | ---- | 3.45x10$^{24}$ | 529 | 7.03 | 47.7 | 2.78 | 6.84 | 4.5 |
| Z.8e | ---- | ---- | ---- | ---- | ---- | 3.87x10$^{24}$ | ---- | 1.46 | 50 | ---- | 0.007 | 0.005 |

Table X. Conditions at ignition, i.e., when fusion energy deposition equals total losses, for the initial conditions of Table IX using the full physics model and selected subsets. Also shown are the maximum values reached in the calculations. Models used: Z.7, 8: full model; (a) no end losses; (b) no end losses and no thermoelectric effect; (c) no end losses and no magnetically enhanced alpha deposition; (d) no end losses and no alpha deposition; (e) no end losses and $B_z$=0. Case Z.7 and variations did not reach ignition. Cases Z.8c, Z.8d, and Z.8e did not reach ignition. Units: $n$—/cm$^3$; $B_z$—MG; $T$—keV; $RB$—MG-cm; yield--MJ.

The major difference between Z.7a and the corresponding Slutz-10 simulation is in density and temperature profile effects that are beyond the scope of our simple model. The Slutz-10 simulations show cooling to the cold pusher with the subsequent increase in density and magnetic field at the outer boundary of the fuel. This boundary layer is qualitatively similar to those reported by Lindemuth et al.[27] who showed that under certain conditions such a boundary layer may be unstable and lead to increased thermal losses; because of the straight field lines in the present case, the layer would be expected to be marginally stable. The formation of the boundary layer both decreases the effective compression of the center and reduces heat losses by providing an insulating boundary. Because of the boundary effects, the on-axis density in the Slutz-10 simulation at maximum compression is approximately 25% of the Z.7a maximum value tabulated in Table XX, the on-axis temperature is 100% higher than the tabulated value, and the pressure is 50% of the tabulated value. *A priori*, we would expect our simple model to be most accurate when all of the fuel is heated adiabatically (in fact, in the Slutz-10 simulations, the central fuel is approximately adiabatically heated but has a compression below that of the pusher compression ratio).

Because of the way the simulations were reported by S&V-12 (e.g., a specific velocity was not reported), it is difficult to make a direct comparison of Z.8a with the S&V-12 results. The Z.8a implosion energy of 3 MJ/cm, the yield of 130 MJ/cm, the convergence of order 25, and a peak density of 3.3 g/cm$^3$ are in the range of the S&V-12 results without cryogenic fuel, although the gain of 43.1 may be higher.

Slutz-10 was the first to call attention to the importance of the thermoelectric (Nernst) effect in this parameter range. As a comparison of Z.7b with Z.7a shows, the thermoelectric effect can reduce the gain by reducing the magnetic field. In Z.7a, 24% of the magnetic flux is lost at peak compression and an additional 21% is lost on the subsequent expansion. The corresponding values for Z.7b are 2% and 9%. The corresponding values for the higher density, more rapid implosion are 17% (Z.8a) and less than 1% (Z.8b) lost at peak compression.

As a comparison of Z.8c with Z.8a, and to a lesser extent a comparison of Z.7c with Z.7a, shows, the magnetic enhancement of alpha deposition is absolutely required for high gain in the density range considered. Z.7d and Z.8d show that a total absence of alpha deposition is not significantly different from having no magnetic enhancement, Z.7c and Z.8c. And, of course, as shown by the zero-field cases Z.7e and Z.8e, without the magnetic reduction in thermal conductivity, the fuel does not heat up significantly and does not build up enough back-pressure to stop the implosion (i.e., a $C_R$=50 is reached, at which the computations are arbitrarily terminated).

## V. CYLINDRICAL TARGETS WITH AZIMUTHAL MAGNETIC FIELD ($B_{\varphi}$)

As opposed to cylindrical targets with an axial magnetic field, cylindrical targets with an azimuthal field do not have to contend with unmagnetized thermal conduction end losses (a discussion of the null field point on axis is beyond the scope of this paper). Therefore, it is anticipated that the length-to-radius ratio can be considerably smaller than in the previous case. It is also anticipated that the practical operating space may be significantly different because of the different dependence of the magnetic field, and hence ωτ, on convergence ratio, as indicated in Table III. As an example of this difference, Figure 6 shows the electron ωτ history for two computations using identical initial conditions, the initial conditions of case Z.2 discussed previously. With an axial magnetic field (Fig. 6A; case Z.2), the ωτ increases rapidly and the temperature correspondingly increases and ignition occurs (Fig. 3B). On the other hand, with the azimuthal field, the magnetic field increases linearly with $C_R$, and the subsequent increase in ωτ is not large enough to sufficiently reduce the thermal conduction. Consequently, the temperature rises to only about 1 keV at a $C_R$ of 10, and then remains approximately constant as the implosion proceeds. Furthermore by $C_R$=10, approximately 50% of the magnetic flux has been lost.

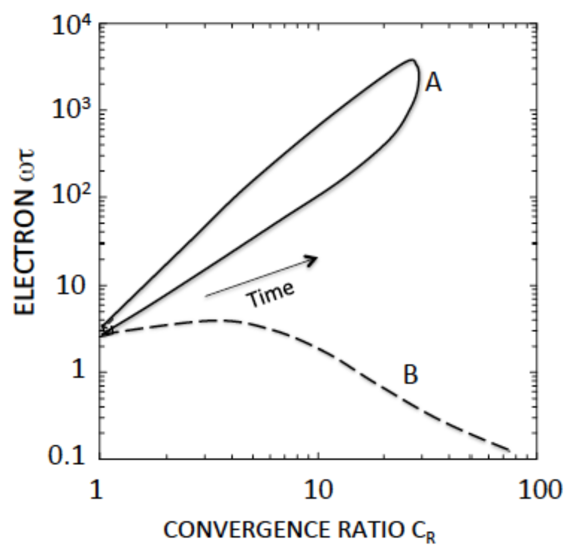


Fig. 6. Variation of electron ωτ for two computations using initial conditions identical to case Z.2 of section III ($n$=4.45 x $10^{20}$/cm$^3$, $T$=250 eV, $B$=334 kG, $R$=0.214 cm, $L$=0.71 cm, $v$=7.5 cm/μs, $E$=670 kJ) and using: (A) axial magnetic field; (B) azimuthal magnetic field.

As an example of the ignition parameter space for cylindrical targets with an azimuthal field, we consider a length-to-radius ratio of 15. The minimum size for ignition and the corresponding $RB$ product is shown in Fig. 7 for $\beta$=1. A comparison of Fig. 7 with Fig. 1 shows that the minimum size and $RB$ product at any given $n$-$T$ point is significantly smaller for the azimuthal field case, except at the very highest density, where the two are comparable.

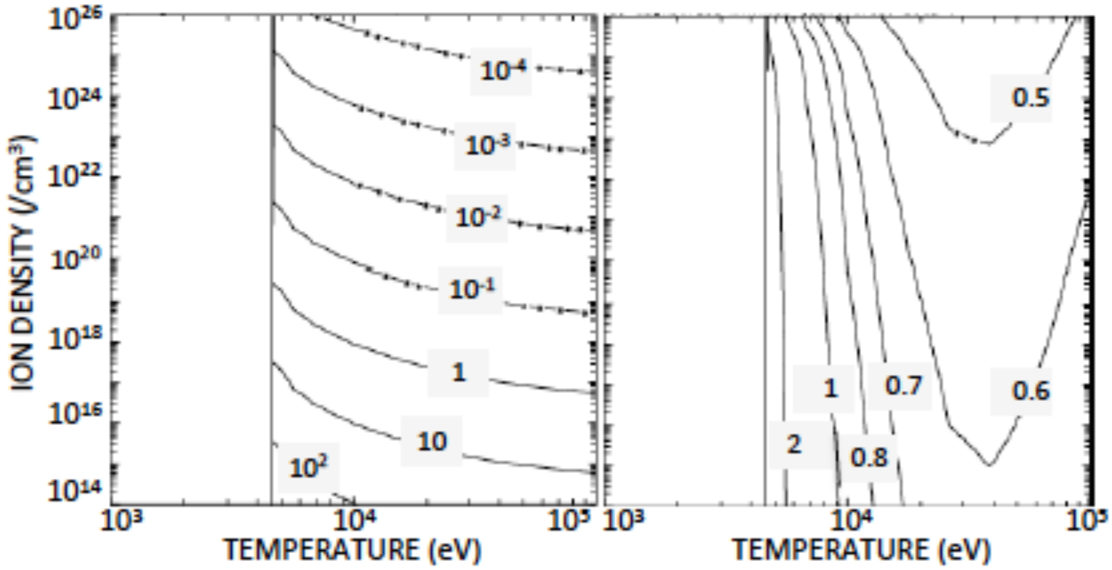


Fig. 7. The minimum radius (left; units-cm) and *RB* product (right; units—MG-cm) for ignition in cylindrical targets with an azimuthal ($B_\varphi$) magnetic field ($L/R$=15, $\beta$=1).

Although at any given density the ignition condition can be reached at a temperature as low as approximately 4.3 keV, we consider a temperature of 7 keV to keep the required *RB* product in the range of 1-2. Fig. 8 shows how the minimum size, minimum plasma energy, and required magnetic field vary with density for different values of $\beta$ at 7 keV.

According to Table III, the *RB* product for this geometry is a constant to the extent that magnetic flux is conserved. Therefore, the initial *RB* product must be the product required at ignition. Whereas the magnetic field for cylindrical $B_z$ targets can be applied by external sources, e.g., coils, a $B_\varphi$ target requires current to flow through the target. The *RB* required at ignition gives an approximate value of the current that must be carried, e.g., an *RB* product of 1 MG-cm implies a current of 5 MA. Although this requirement potentially presents a technological challenge, we note that the MAGO chamber, which is either cylindrically or quasi-spherically imploded, has a plasma formation current of approximately 8 MA.[28]

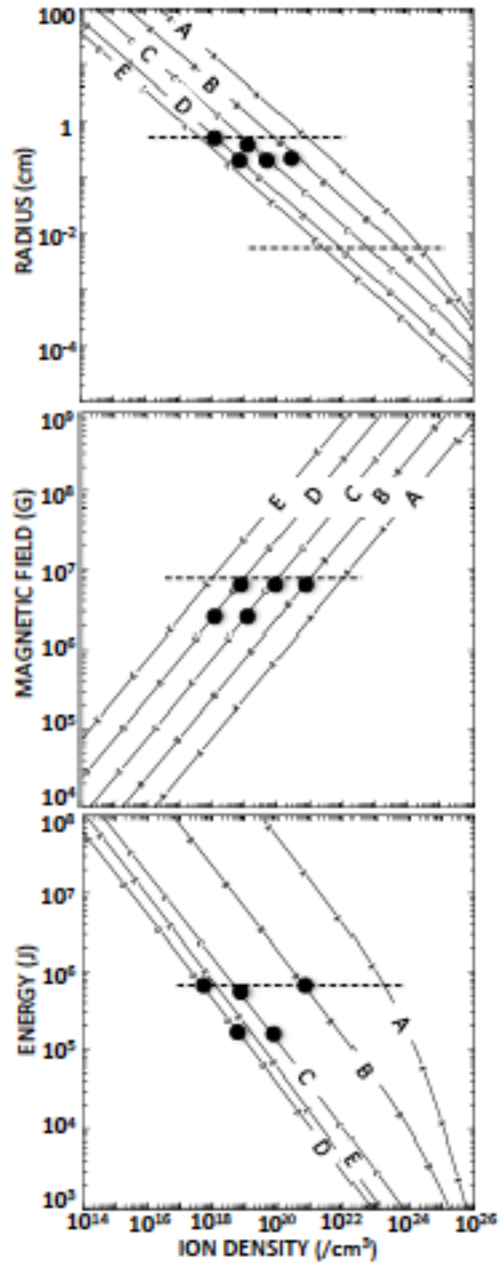


Fig. 8. The minimum radius (top), corresponding magnetic field (middle) and required sum of fuel thermal and magnetic energy (bottom) for ignition at 7 keV as a function of ion density for β at ignition equal to 100 (A), 10 (B), 1 (C), 0.1 (D), and 0.01 (E) for cylindrical targets with an azimuthal ($B_\varphi$) magnetic field ($L/R$=15). The dotted lines show the approximate practical limits on size, energy, and magnetic field as discussed in the text. The solid dots indicate cases Φ.1-5 considered in the text.

Analogous to the case of the axial magnetic field, Figure 8 and practical limits allow us to place approximate bounds on the parameter space in which cylindrical $B_\varphi$

targets can operate. As before, we postulate that ignition should occur at approximately $C_R$=15, the initial size should lie between 0.1 cm and 10 cm, the sum of magnetic and plasma energies at ignition should be less than 500 kJ, and the required initial magnetic field should be less than 500 kG. According to Table III, the latter condition limits the magnetic field for ignition at $C_R$=15 to 7.5 MG. And, as with the previous $B_z$ case, the compressed radius should lie between 0.0067 cm and 0.67 cm. The dotted lines on Fig. 8 indicate these limits. Table XI shows the impact of the limits and indicates an operational range of $10^{18}$-$10^{21}$/cm$^3$ (4.18 x $10^{-6}$-4.18 x $10^{-3}$ g/cm$^3$) depending upon β. A comparison of table XI with table IV shows that the upper end of the operational range of $B_\varphi$ targets is more than an order of magnitude lower in density than the lower end of the operating range of $B_z$ targets.

| Condition\β | 0.01 | 0.1 | 1 | 10 | 100 |
|---|---|---|---|---|---|
| Size | 3x$10^{17}$-$10^{21}$ | $10^{18}$-$10^{22}$ | $10^{19}$-3x$10^{22}$ | $10^{20}$-$10^{23}$ | $10^{21}$-$10^{24}$ |
| Energy | >3x$10^{18}$ | >$10^{18}$ | >$10^{19}$ | >$10^{21}$ | >$10^{23}$ |
| Magnetic field | <$10^{18}$ | <$10^{19}$ | <$10^{20}$ | <$10^{21}$ | <$10^{22}$ |
| Overall | ---- | $10^{18}$-$10^{19}$ | $10^{19}$-$10^{20}$ | $10^{21}$ | ---- |

Table XI. Approximate ignition density range (/cm$^3$) for cylindrical targets with azimuthal magnetic field ($B_\varphi$) at 7 keV based upon compressed size (0.0067-0.67 cm), compressed energy less than 500 kJ, and compressed magnetic field less than 7.5 MG ($L/R$=15).

As examples of $B_\varphi$ target implosions, we will consider the examples shown in Table XII; these cases are shown as dots on Fig. 8. These examples meet the practical conditions on size, magnetic field, and energy.

| | Ignition conditions | | | | | | | | Initial conditions | | | | |
|---|---|---|---|---|---|---|---|---|---|---|---|---|---|
| Case | $n$ | $B_\varphi$ | $R$ | $L$ | $RB$ | $M$ | $E_{ig}$ | $\beta$ | $n$ | $\rho$ | $B_\varphi$ | $R$ | $\beta$ |
| Φ.1 | $10^{18}$ | 2.37 | 0.58 | 8.70 | 1.37 | 0.038 | 443 | 0.1 | 4.45 x $10^{15}$ | 1.86x$10^{-5}$ | 0.16 | 8.70 | 0.003 |
| Φ.2 | $10^{19}$ | 7.51 | 0.18 | 2.67 | 1.35 | 0.011 | 128 | 0.1 | 4.45 x $10^{16}$ | 1.86x$10^{-4}$ | 0.50 | 2.67 | 0.003 |
| Φ.3 | $10^{19}$ | 2.37 | 0.49 | 7.35 | 1.16 | 0.23 | 435 | 1 | 4.45 x $10^{16}$ | 1.86x$10^{-4}$ | 0.16 | 7.35 | 0.027 |
| Φ.4 | $10^{20}$ | 7.51 | 0.15 | 2.26 | 1.13 | 0.067 | 126 | 1 | 4.45 x $10^{17}$ | 1.86x$10^{-3}$ | 0.50 | 2.26 | 0.027 |
| Φ.5 | $10^{21}$ | 7.51 | 0.14 | 2.15 | 1.05 | 0.57 | 527 | 10 | 4.45 x $10^{18}$ | 1.86x$10^{-2}$ | 0.50 | 2.15 | 0.27 |

Table XII. Ignition condition examples at 7 keV and corresponding initial conditions for cylindrical targets with azimuthal magnetic field ($B_\varphi$) under the assumptions of adiabaticity and flux conservation ($C_R$=15, compressed $L/R$=15). The ignition energy $E_{ig}$ is the sum of fuel thermal and magnetic energies. The corresponding initial temperature is 189 eV. Units: $n$—/cm$^3$; $\rho$—mg/cm$^3$; $B_\varphi$—MG; $R,L$—cm; $RB$—MG-cm; fuel mass $M$—mg; $E_{ig}$—kJ.

As in Section III, a series of gain optimization computations was performed to determine the initial velocity and kinetic energy for the $n$-$T$-$B$-$R$ values specified in

Table XII. The results of the optimization and the corresponding computed results are tabulated in Table XIII.

| | Initial | | At ignition | | | | | Maximum | | | | |
|---|---|---|---|---|---|---|---|---|---|---|---|---|
| Case | $v$ | $E$ | $n$ | $B_\varphi$ | $RB$ | $T_i$ | $C_R$ | $n$ | $B_\varphi$ | $T_i$ | $C_R$ | Gain |
| Φ.1 | 0.15 | 0.6 | $5.02 \times 10^{17}$ | 1.68 | 1.34 | 8.01 | 10.6 | $4.13 \times 10^{18}$ | 4.80 | 37.2 | 30.5 | 0.07 |
| Φ.2 | 0.3 | 0.4 | $4.52 \times 10^{18}$ | 5.01 | 1.32 | 8.26 | 10.1 | $3.36 \times 10^{19}$ | 13.7 | 36.0 | 27.5 | 0.5 |
| Φ.3 | 0.2 | 1.5 | $3.39 \times 10^{18}$ | 1.38 | 1.14 | 7.75 | 8.86 | $3.35 \times 10^{19}$ | 4.27 | 43.9 | 27.5 | 1.48 |
| Φ.4 | 0.6 | 0.5 | $3.36 \times 10^{19}$ | 4.28 | 1.11 | 7.44 | 8.69 | $3.63 \times 10^{20}$ | 14.0 | 46.1 | 28.6 | 1.41 |
| Φ.5 | 1 | 2 | $9.47 \times 10^{20}$ | 7.26 | 1.07 | 7.24 | 14.6 | $3.34 \times 10^{21}$ | 13.3 | 31.5 | 27.4 | 10.1 |

Table XIII. Initial velocity $v$ and initial kinetic energy $E$ that approximately maximize gain for the initial $n$, $B_\varphi$, and $R$ specified in Table XII and an initial temperature of 189 eV. Also shown are subsequent conditions at ignition, i.e., when fusion energy deposition rate equals total loss rate. Also shown are the maximum values reached in the computations. Units: $v$—cm/μs; $E$—MJ; $n$—/cm$^3$; $B_\varphi$—MG; $RB$—MG-cm; $T_i$—keV.

A comparison of the velocity and energy in Table XIII with the same quantities in table VII indicates that the $B_\varphi$ targets operate at a significantly lower velocity, a consequence of the lower density. Because the density is lower, the fusion reaction rates are correspondingly smaller, leading to a requirement of longer burn time, hence a slower implosion and the correspondingly longer dwell time.

Table XIII shows two perhaps surprising results for examples Φ.1, 2, 3 and 4: the ignition condition is reached at a significantly smaller value of $C_R$ than the targeted value of 15, and, in spite of reaching ignition, the gain is quite small compared with the examples in section III.

Fig. 9 shows the temperature history for cases Φ.1, Φ.3 and Φ.5. Φ.1 (Fig. 9A) and Φ.3 (Fig. 9B) increase more rapidly than adiabatic in the early phase of the implosion due to Ohmic and thermoelectric heating that initially exceeds the compressional heating. Because the initial $\beta$ is so low, only a relatively small loss of magnetic energy due to Ohmic and thermoelectric flux losses can change the thermal energy significantly. Only Φ.5 increases approximately adiabatically. The behavior of Φ.1 and Φ.3 near peak compression differs from Φ.5 in that Φ.1 and Φ.3 do not show a substantial increase in temperature during the dwell period. Even though the ignition condition is exceeded (Table XIII), the fuel does not burn rapidly enough to give a rapid increase in temperature. This is consistent with the previous findings of L&K-83, who explored the effect of 100% alpha deposition and noted "the fact that the new region is not significantly affected reflects the relatively slow burn times that occur in slowly driven magnetized fuel targets. The alpha deposition rates do not substantially exceed the other heating and loss rates." Only Φ.5 shows the characteristic increase in temperature.

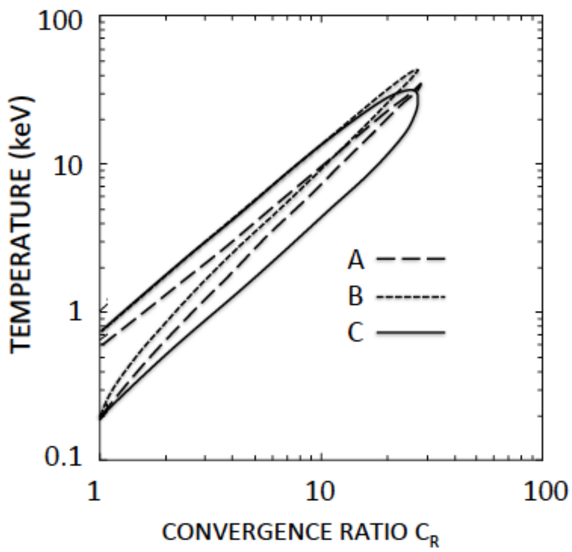

Fig. 9. The ion temperature history of cases Φ.1 (A), Φ.3 (B) and Φ.5 (C). Time increases counterclockwise from the initial temperature value of 189 eV.

For cases Φ.1-Φ.5, less than 5% of the magnetic flux is lost during the implosion and subsequent expansion. Radiation losses reach somewhat more than 100% of the conduction losses for Φ.1 and Φ.2 and only about 60% for Φ.3, Φ.4, and Φ.5. End losses are initially about 60-70% of the total conduction losses and decrease to less than 5% at maximum compression. The thermoelectric conduction losses are initially about 90%, 60%, and 15% of the total conduction losses for cases Φ.1 and Φ.2, Φ.3 and Φ.4, and Φ.5, respectively, and decrease to 5%, 1% and 0.1% at maximum compression.

The low gain of Φ.4 (and Φ.1, 2, 3) raises the question of whether or not high gain can be achieved with an initial density as low as 4.45 x $10^{17}$/cm$^3$. We have tried many combinations of initial parameters, including exceeding the practical limitations, and find no more than a factor of 2 or 3 can be obtained while maintaining the convergence less than 30. Only an increase in initial density or an increase in convergence can lead to a significant increase in gain.

The cases considered here have an initial $L/R$ of unity, based upon an ignition $C_R$ and $L/R$ of 15. Table XIV shows how the ignition dimensions and energy depend upon the $L/R$ ratio. For any $L/R$ greater than 5, the minimum radius and the energy per unit length remains essentially constant. This indicates that for a given $n$-$T$-$B$ combination, the required energy could be less than indicated in Fig. 8, thereby potentially opening up the operating space somewhat, particularly to higher density and β. However, there may be practical limits on the initial $L/R$. If, for example, the $L/R$ is 5 at $C_R$=15, the initial $L/R$ is 0.33. Furthermore, at the smaller $L/R$ ratios, it is difficult to find ignition conditions at a density higher than $10^{21}$/cm$^3$ that simultaneously satisfy all practical limitations. For example, at 3 x $10^{21}$/cm$^3$, 7 keV, $\beta$=32 ($B_\varphi$=7.3 MG), and $L/R$=4, the initial magnetic field is 487 kG and the ignition energy (sum of magnetic and thermal) is 435 kJ. At higher β, the energy increases to a value above the postulated limit, whereas, at lower β, the initial magnetic field increases above the postulated limit.

| $L/R$ | $R$(cm) | $L$(cm) | $E_{ig}$ (kJ) | $E_{ig}/L$ (kJ/cm) |
|---|---|---|---|---|
| 2 | 0.162 | 0.323 | 101 | 313 |
| 5 | 0.146 | 0.730 | 186 | 255 |
| 10 | 0.144 | 1.44 | 355 | 247 |
| 15 | 0.143 | 2.15 | 527 | 245 |
| 25 | 0.143 | 3.57 | 874 | 245 |
| 40 | 0.143 | 5.71 | 1395 | 244 |

Table XIV. Dependence of ignition size and energy required on $L/R$ ratio for $n$=$10^{21}$/cm$^3$, $T$=7 keV, $B_\varphi$=7.51 MG (β=10). An $L/R$ of 15 corresponds to case Φ.5.

The cases so far considered in this section and Section III have used initial conditions projected to reach ignition at a temperature of 7 keV. For the cylindrical $B_z$ targets considered in Section III, a temperature of 7 keV was chosen because the minimum ignition size occurred at approximately this temperature (Fig. 1). However, for cylindrical $B_\varphi$ targets, Fig. 7 shows that the minimum size, and hence minimum thermal energy, decreases with increasing temperature, although the required minimum magnetic field increases to maintain the same $\beta$. The net reduction in energy required from the driver changes the overall density limits of Table XI, in general leading to somewhat lower minimum and maximum densities at the same $\beta$, or, correspondingly, allowing operation at a higher $\beta$ for a given density. Offsetting this potential advantage is a fact that an increased ignition temperature also requires an increased initial temperature to maintain the same ignition $C_R$ and the increased initial pressure potentially increases the driver requirements.

Table XV summarizes calculations that were performed using initial conditions projected back from an ignition temperature of 15 keV. As with the previous calculations, the initial velocity and energy are chosen to approximately maximize the gain achieved with the specified initial conditions. A comparison of the cases in Table XV with cases Φ.3, Φ.4, and Φ.5 show that, for a given initial density (or given targeted ignition density), the required velocity and energy, and the subsequent gains, are comparable. Based upon these results, there does not appear to be any advantage in choosing an ignition temperature of 15 keV that offsets the required increased initial temperature of 405 eV.

| | Ignition conditions | | | | | | | | Initial conditions | | | | |
|---|---|---|---|---|---|---|---|---|---|---|---|---|---|
| Case | $n$ | $B_\varphi$ | $R$ | $L$ | $RB$ | $M$ | $E_{ig}$ | $\beta$ | $n$ | $\rho$ | $B_\varphi$ | $R$ | $\beta$ |
| Φ.6 | $10^{19}$ | 3.48 | 0.19 | 2.84 | 0.66 | 0.013 | 54 | 1 | $4.45 \times 10^{16}$ | $1.86\times10^{-4}$ | 0.23 | 2.84 | 0.027 |
| Φ.7 | $10^{20}$ | 3.48 | 0.18 | 2.72 | 0.63 | 0.12 | 230 | 10 | $4.45 \times 10^{17}$ | $1.86\times10^{-3}$ | 0.23 | 2.72 | 0.27 |
| Φ.8 | $10^{21}$ | 6.31 | 0.097 | 1.45 | 0.61 | 0.18 | 323 | 30 | $4.45 \times 10^{18}$ | $1.86\times10^{-2}$ | 0.42 | 1.45 | 0.82 |

| | Initial | | At ignition | | | | | Maximum | | | | |
|---|---|---|---|---|---|---|---|---|---|---|---|---|
| Case | $v$ | $E$ | $n$ | $B_\varphi$ | $RB$ | $T_i$ | $C_R$ | $n$ | $B_\varphi$ | $T_i$ | $C_R$ | Gain |
| Φ.6 | 0.3 | 140 | $7.00 \times 10^{18}$ | 2.88 | 0.65 | 17.2 | 12.5 | $3.48 \times 10^{19}$ | 6.41 | 52.1 | 28.0 | 0.28 |
| Φ.7 | 0.4 | 700 | $9.37 \times 10^{20}$ | 3.30 | 0.62 | 16.3 | 14.5 | $2.68 \times 10^{20}$ | 5.58 | 33.2 | 24.5 | 2.39 |
| Φ.8 | 1.5 | 1000 | $1.07 \times 10^{21}$ | 6.43 | 0.60 | 15.5 | 15.5 | $3.62 \times 10^{21}$ | 11.8 | 36.6 | 28.5 | 4.79 |

Table XV. Targeted ignition conditions and corresponding initial conditions ($C_R$ = 15, $T$=15 keV, $L/R$=15; top) and computed initial, ignition, and maximum conditions (bottom) for cylindrical targets with azimuthal magnetic field ($B_z$) and an initial temperature of 406 eV. Units: $n$—/cm$^3$; ρ—mg/cm$^3$; $B_\varphi$—MG; $T$--keV; $R,L$—cm; $RB$—Mg-cm; $v$—cm/us; fuel mass $M$—mg; $E$—kJ.

As with the cylindrical targets with an axial magnetic field, it is reasonable to ask whether or not ignition can be obtained at lower convergence ratios. A $C_R$ =10 changes the initial size range to 0.01-1 cm and reduces the maximum magnetic field to 5 MG. An examination of Fig. 8 shows that these limitations can be met for a compressed density less than approximately $10^{20}$/cm$^3$. Similarly, the limitations at $C_R$ =7.5 can be met for a compressed density less than about 3 x $10^{19}$/cm$^3$. However, Table XIII suggests only a gain of unity or so can be obtained at these low densities, and this has been confirmed with corresponding calculations.

The initial conditions for the cases considered so far have been based upon the minimum size, and hence minimum mass and energy, that meet the ignition conditions for a specific density, temperature (i.e., 7 keV), $\beta$ and $C_R$ =15. As we have shown, using initial conditions projected back from the ignition conditions provides a reasonable starting point but optimum gain may be achieved with some variation in the parameters (e.g., Fig. 4). Table XVI summarizes a computation where the initial $L/R$ radius was 0.4 and, because of the high initial temperature, ignition occurred at a $C_R$ of 9.63, i.e., an $L/R$ of 3.85. The minimum mass for ignition with this parameter set is 0.76 mg, so case Φ.9 has twice the minimum mass.

|  | Initial conditions |  |  |  |  |  |  |  |  |  | Projected at 7 keV |  |  |  |  |
|---|---|---|---|---|---|---|---|---|---|---|---|---|---|---|---|
| Case | $n$ | $\rho$ | $B_\varphi$ | $T$ | $R$ | $L$ | $M$ | $v$ | $E$ | β | $C_R$ | $n$ | $B_\varphi$ | $RB$ | $\beta$ |
| Φ.9 | 2.4 x $10^{18}$ | $10^{-2}$ | 0.3 | 0.5 | 5 | 2 | 1.56 | 0.3 | 4 | 1.07 | 7.2 | 1.26 x $10^{20}$ | 2.17 | 1.51 | 15 |

|  | At ignition |  |  |  |  | Maximum |  |  |  |  |
|---|---|---|---|---|---|---|---|---|---|---|
| Case | $n$ | $B_\varphi$ | $RB$ | $T_i$ | $C_R$ | $n$ | $B_\varphi$ | $T_i$ | $C_R$ | Gain |
| Φ.9 | 2.2 x $10^{20}$ | 2.74 | 1.42 | 6.2 | 9.63 | 3.67 x $10^{20}$ | 3.51 | 59.3 | 12.4 | 30.3 |

Table XVI. Initial, ignition, and maximum conditions for a high-gain, low convergence cylindrical target with azimuthal magnetic field ($B_\varphi$). Units: $n$—/cm$^3$; $\rho$—mg/cm$^3$; $B_\varphi$—MG; $T$--keV; $R,L$—cm; $RB$—Mg-cm; $v$—cm/us; fuel mass $M$—mg; $E$—MJ.

Fig. 10 shows how the gain and convergence vary with initial parameters for case Φ.9. As with case Z.2 (Fig. 4), a wide range of parameters can lead to a gain within a factor of, say, 2 of the maximum, suggesting again that magnetized targets are potentially quite robust. For this example, when ignition and high gain are achieved, the convergence is limited to quite low value, possibly even less than 10 (Fig. 10B and C). On the other hand, when ignition and high gain are not achieved, the fuel/magnetic pressure does not build up large enough to keep the pusher from going to large convergences.

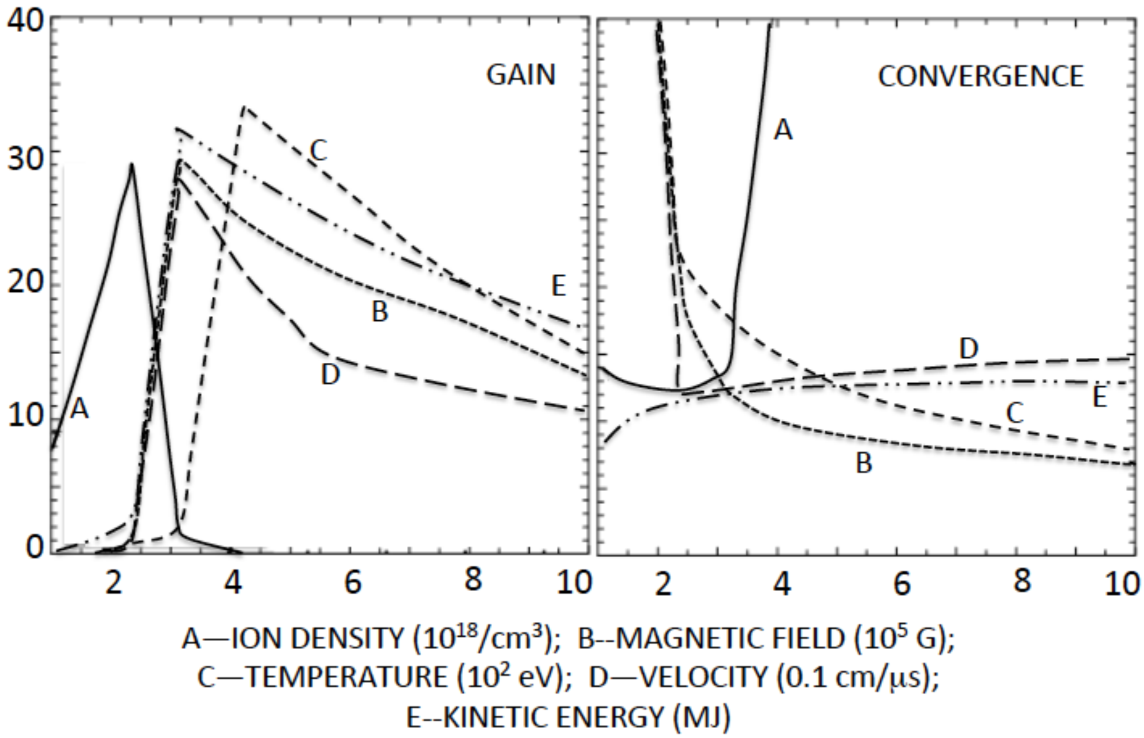


Fig. 10. The variation of gain (left) and convergence ratio (right) with variation in initial parameters for a basic cylindrical high gain, low convergence target parameter set of $n$=2.4 x $10^{18}$/cm$^3$, $T$=500 eV, $B_\varphi$=300 kG, $R$=5 cm, $L$=2 cm, $v$=0.3 cm/μs, $E$=4 MJ (case Φ.9).

Compared to the targets with axial magnetic field, the initial target plasmas discussed in this section all have very low $\beta$, ranging from 0.003 to 1.1, and low initial density, ranging from 4.5 x $10^{15}$/cm$^3$ to 4.5 x $10^{18}$/cm$^3$. For gain much greater than unity, an initial density greater than $10^{18}$/cm$^3$ is required. Formation of magnetized plasmas in this $\beta$-$n$ range with 189 eV-500 eV initial temperature represents a formidable challenge. On the other hand, the driver requirements (0.15-1 cm/μs, 0.4-4 MJ) are in or near the range that has already demonstrated experimentally with magnetically driven liners. As example Φ.9 shows, $B_\varphi$ cylindrical targets have the potential of achieving high gain at very low convergence levels.

An example of a cylindrical target involving an azimuthal magnetic field is the staged z-pinch, in which a magnetically driven argon liner compresses a fusion fuel.[29] This concept appears to be predicated on radial convergences (e.g., 100) much greater than deemed practical in this paper. Furthermore, the target plasma is initially unmagnetized but becomes somewhat magnetized during the implosion as magnetic field diffuses through the liner. However, much of the target plasma appears to be unmagnetized, and reported values of density, temperature, and magnetic field suggest that the electron $\omega\tau$ of any of the fusion fuel is not much larger than unity. Therefore, in the context of this paper, it is not clear that the staged z-pinch can be called a magnetized target.

Information provided in reference 29 about the target plasma during the implosion allows a comparison with our model. At 122 ns, the paper gives average values approximately equal to the following: $R$=0.02 cm, $n$=2.3 x $10^{23}$/cm$^3$, $T$=120 eV, $B$=34 MG (actually, this field value is the peak, not average). The authors note that the target is "optically thin," so, for these values, radiation is the dominant loss mechanism if the radiation is simple Bremmstrahlung. Eq. 17 of L&S-09 for these parameters suggests that a velocity of 10 cm/μs is required just to offset the total losses. Similarly, for the profiles at 124 μs and 124.5 μs, a velocity of approximately 15 and 19 cm/μs would be required. Presumably, a significantly higher velocity would be required to actually result in heating. Although the authors do not actually state a target implosion velocity, the timing of the implosion suggests that the implosion velocity is probably less than 10 cm/μs (as examples, the implosion covers 1.2 mm from 100 ns to 122 ns and 0.18 mm from 122 ns to 125 ns, for average velocities of 5.5 cm/μs and 6 cm/μs, respectively).

We have performed a calculation using the 122 ns values noted in the previous paragraph, a kinetic energy of 1 MJ as taken from reference 29, and an initial velocity of 7 cm/μs. During the implosion, the velocity reaches a maximum of 8 cm/μs. These values lead to an implosion that reaches a $C_R$=9.8 at 124.8 ns, both consistent with values reported in reference 29. Because of the high radiation rates, the radiation temperature builds up sufficiently to reduce the actual loss rate to about 10-20% of the simple Bremmstrahlung rate. However, even with the reduced radiation losses, the plasma in our computations heats up to only about 600 eV and gives essentially negligible yield, in stark contrast with the reported simulations. Without further information on the radiation model and the velocity achieved in the reported simulations, it is impossible to resolve these differences. It may be possible that the details of the temperature, density, and magnetic field radial profiles can explain the differences. Since the reported simulations show little two-dimensional behavior at 122 ns, and since the authors report that the yield is decreased by only a factor of 50% in the two-dimensional simulations, it is doubtful that two-dimensional effects can resolve the differences.

## VI. SPHERICAL TARGETS WITH AZIMUTHAL MAGNETIC FIELD ($B_\varphi$)

Spherical targets, of course, do not have end effects (again, the issue of a magnetic field null on the axis is beyond the scope of this paper). Fig. 11 shows the ignition parameter space for β=1. This parameter space is quite similar to that of the $B_\varphi$ cylindrical targets (Fig. 7).

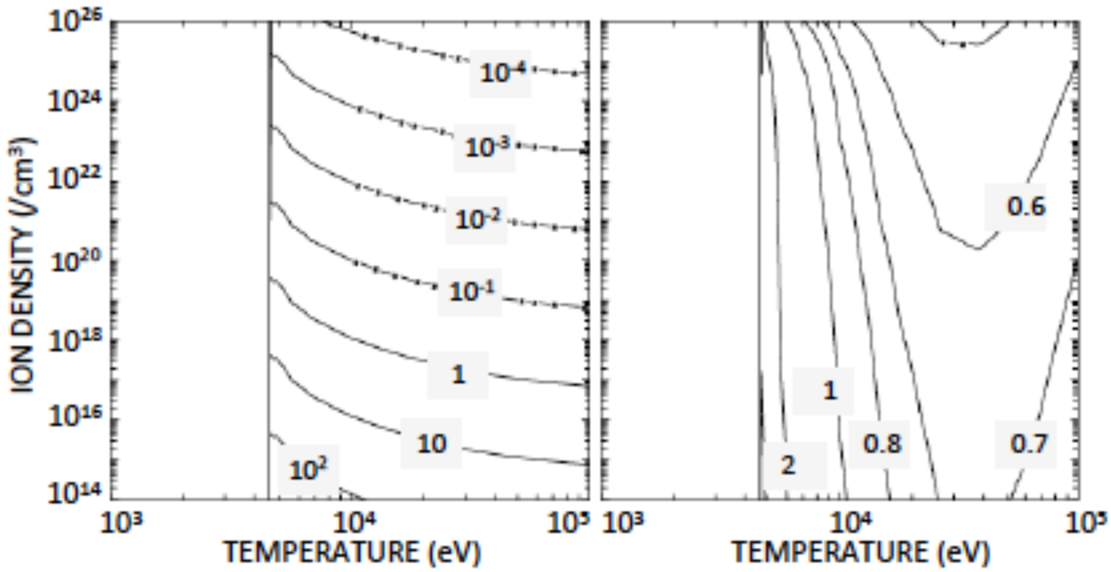


Fig. 11. The minimum ignition radius (left; units-cm) and *RB* product (right; units—MG-cm) for ignition in spherical targets with an azimuthal ($B_\varphi$) magnetic field (β=1).

As in the previous cylindrical $B_z$ and $B_\varphi$ cases, postulated practical limits can be used to define the potential operating space. As with the cylindrical $B_z$ case, the magnetic field in spherical targets increases as $C_R^2$, so the upper limit on the magnetic field at $C_R$ =15 is 112 MG. Fig. 12 and Table XVII show the operating space. Table XVII shows that the overall potential operating space for spherical targets is much greater than for either of the cylindrical targets, covering a density range from approximately $10^{17}$/cm$^3$ (4.18 x $10^{-7}$ g/cm$^3$) to approximately $10^{24}$/cm$^3$ (4.18 g/cm$^3$). Furthermore, the postulated magnetic field and energy limits do not restrict the parameter space whatsoever.

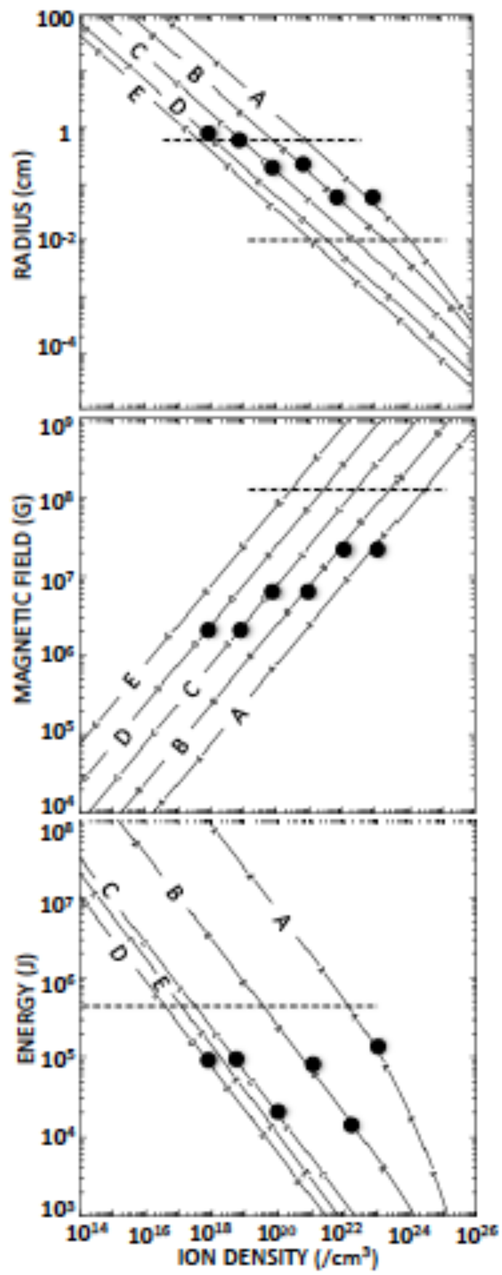


Fig. 12. The minimum ignition radius (top), corresponding magnetic field (middle) and required sum of fuel thermal and magnetic energy (bottom) for ignition at 7 keV as a function of ion density for $\beta$ equal to 100 (A), 10 (B), 1 (C), 0.1 (D), and 0.01 (E) for spherical targets with an azimuthal ($B_\varphi$) magnetic field. The dotted lines show the approximate practical limits on size, energy, and magnetic field as discussed in the text. The solid dots indicate cases S.1-6 considered in the text.

| Condition\β | 0.01 | 0.1 | 1 | 10 | 100 |
|---|---|---|---|---|---|
| Size | $10^{17}$-$10^{21}$ | $10^{18}$-3x$10^{21}$ | $10^{19}$-3x$10^{22}$ | $10^{20}$-3x$10^{23}$ | $10^{21}$-$10^{24}$ |
| Energy | >$10^{13}$ | >$10^{14}$ | >3x$10^{16}$ | >3x$10^{19}$ | >$10^{22}$ |
| Magnetic field | <3x$10^{20}$ | <3x$10^{21}$ | <3x$10^{22}$ | <3x$10^{23}$ | <3x$10^{24}$ |
| Overall | $10^{17}$-3x$10^{20}$ | $10^{18}$-3x$10^{21}$ | $10^{19}$-3x$10^{22}$ | $10^{20}$-3x$10^{23}$ | $10^{21}$-$10^{24}$ |

Table XVII. Approximate compressed density range (/cm$^3$) for spherical targets with azimuthal magnetic field ($B_\varphi$) at 7 keV based upon compressed size (0.0067-0.67 cm), compressed magnetic and thermal energy less than 500 kJ, and compressed magnetic field less than 113 MG.

Table XVIII gives examples for which computations have been performed. Table XIX summarizes the results. A comparison of Table XVIII with Tables XII and VI shows that the energy required for ignition is much smaller than required for the cylindrical geometries. The larger initial radii are comparable to those of the $B_\varphi$ cylindrical targets and the smaller radii are larger than that of the $B_z$ targets. The range of initial velocities (Table XIX) covers much of the range of both types of cylindrical targets.

| | Ignition conditions | | | | | | | Initial conditions | | | | |
|---|---|---|---|---|---|---|---|---|---|---|---|---|
| Case | $n$ | $B_\varphi$ | $R$ | $RB$ | $M$ | $E_{ig}$ | $\beta$ | $n$ | $\rho$ | $B_\varphi$ | $R$ | $\beta$ |
| S.1 | $10^{18}$ | 2.37 | 0.66 | 1.56 | 0.005 | 75.5 | 0.1 | 2.96 x $10^{14}$ | 1.24x$10^{-6}$ | 0.011 | 9.93 | 0.007 |
| S.2 | $10^{19}$ | 2.37 | 0.56 | 1.33 | 0.030 | 66.6 | 1 | 2.96 x $10^{15}$ | 1.24x$10^{-5}$ | 0.011 | 8.34 | 0.067 |
| S.3 | $10^{20}$ | 7.51 | 0.17 | 1.28 | 0.009 | 19.1 | 1 | 2.96 x $10^{16}$ | 1.24x$10^{-4}$ | 0.033 | 2.55 | 0.067 |
| S.4 | $10^{21}$ | 7.51 | 0.16 | 1.20 | 0.073 | 69.8 | 10 | 2.96 x $10^{17}$ | 1.24x$10^{-3}$ | 0.033 | 2.42 | 0.67 |
| S.5 | $10^{22}$ | 23.7 | 0.049 | 1.16 | 0.021 | 19.6 | 10 | 2.96 x $10^{18}$ | 0.0124 | 0.106 | 0.736 | 0.67 |
| S.6 | $10^{23}$ | 23.7 | 0.044 | 1.04 | 0.144 | 119.0 | 100 | 2.96 x $10^{19}$ | 0.124 | 0.106 | 0.654 | 6.668 |

Table XVIII. Ignition condition examples at 7 keV and corresponding initial conditions for spherical targets with azimuthal magnetic field ($B_\varphi$) under the assumptions of adiabaticity and flux conservation ($C_R$=15). The ignition energy $E_{ig}$ is the sum of fuel thermal and magnetic energies. The corresponding initial temperature is 31.1 eV. Units: $n$—/cm$^3$; ρ mg/cm$^3$; $B_\varphi$ —MG; $R$—cm; RB MG-cm; fuel mass $M$—mg; $E_{ig}$—kJ.

| | Initial | | At ignition | | | | | Maximum | | | | | |
|---|---|---|---|---|---|---|---|---|---|---|---|---|---|
| Case | $v$ | $E$ | $n$ | $B_\varphi$ | $RB$ | $T_i$ | $C_R$ | $n$ | $B_\varphi$ | $RB$ | $T_i$ | $C_R$ | Gain |
| S.1 | 0.1 | 300 | 5.69x10$^{17}$ | 1.60 | 1.28 | 10.0 | 12.4 | 5.38x10$^{18}$ | 7.16 | 2.70 | 55.4 | 26.3 | 0.07 |
| S.2 | 0.3 | 300 | 3.98x10$^{18}$ | 1.23 | 0.93 | 10.1 | 11.0 | 4.72x10$^{19}$ | 6.36 | 2.11 | 70.3 | 25.0 | 1.18 |
| S.3 | 0.6 | 80 | 3.79x10$^{19}$ | 3.70 | 0.87 | 10.9 | 10.9 | 3.56x10$^{20}$ | 16.4 | 1.93 | 66.4 | 22.9 | 1.52 |
| S.4 | 1 | 200 | 2.11x10$^{21}$ | 10.3 | 1.30 | 6.87 | 19.2 | 6.87x10$^{21}$ | 22.6 | 1.92 | 62.6 | 28.5 | 20.4 |
| S.5 | 3 | 60 | 1.37x10$^{22}$ | 25.3 | 1.12 | 7.72 | 16.6 | 4.59x10$^{22}$ | 56.5 | 1.67 | 54.1 | 24.9 | 16.3 |
| S.6 | 5 | 400 | 3.00x10$^{23}$ | 40.7 | 1.23 | 5.88 | 21.6 | 6.16x10$^{23}$ | 65.4 | 1.55 | 122 | 27.5 | 49.9 |

Table XIX. Initial velocity $v$ and initial kinetic energy $E$ that approximately maximize gain for the initial $n$, $B_\varphi$, $T$, and $R$ specified in Table XVIII. Also shown are conditions at ignition, i.e., when fusion energy deposition rate equals total loss rate. Also shown are the maximum values reached in the computations. Units: $v$—cm/μs; $E$—kJ; $n$—/cm$^3$; $B_\varphi$ —MG; $RB$—Mg-cm; $T_i$—keV.

As with the lower-density, lower-$\beta$ $B_\varphi$ cylindrical targets, there are cases where Ohmic/thermoelectric heating initially exceeds or is comparable to the hydrodynamic work so that the temperature initially increases faster than adiabatic. For all cases except S.6 Ohmic/thermoelectric heating exceeds about 10% of the hydrodynamic work rate until about $C_R$=2. For the lower initial densities, the thermoelectric conduction loss rate is initially dominant, being approximately 90% of the total conduction loss rate for S.1 and decreasing to less than 10% at maximum compression. For S.6, the thermoelectric losses are initially only 10% of the total. For all cases, radiation losses are initially less than 10% of the conduction losses but increase relatively and exceed the conduction losses at peak compression.

As with the previously discussed targets, ignition and high gain is achieved at very low $\rho R$ compared to conventional unmagnetized targets. S.4 reaches a maximum $\rho R$ of only 0.002 g/cm$^2$ and S.6 reaches 0.06 g/cm$^2$. And as with the $B_\varphi$ cylindrical targets, there are cases (S.1, 2, 3) where the gain is low even though the ignition condition is reached; in these cases, the maximum alpha deposition rate is less than or comparable to the hydrodynamic rate and is not able to significantly overcome the hydrodynamic cooling as the implosion reaches maximum compression and begins to expand (e.g., for S.1, the peak deposition rate is 6.9x10$^8$ W, whereas the hydrodynamic work rate exceeds 10$^{10}$ W during the implosion).

Figures 13 and 14 show how the gain and convergence varies for cases S5 (a low-energy case) and S6 (a high-energy case), respectively, with changes in any initial parameter. For the former, either an increase in density, a decrease in magnetic field, or a decrease in velocity can lead to a gain over 30. For the latter, similar changes in initial density and field, as well as a decrease in initial kinetic energy, can lead to a gain over 70, and a decrease in velocity can lead to a gain over 50. These figures, along with Figures 4 and 10, illustrate that the set of initial parameters determined by projecting back from ignition conditions provide a reasonable starting point but some variation in those parameters may lead to a higher gain.

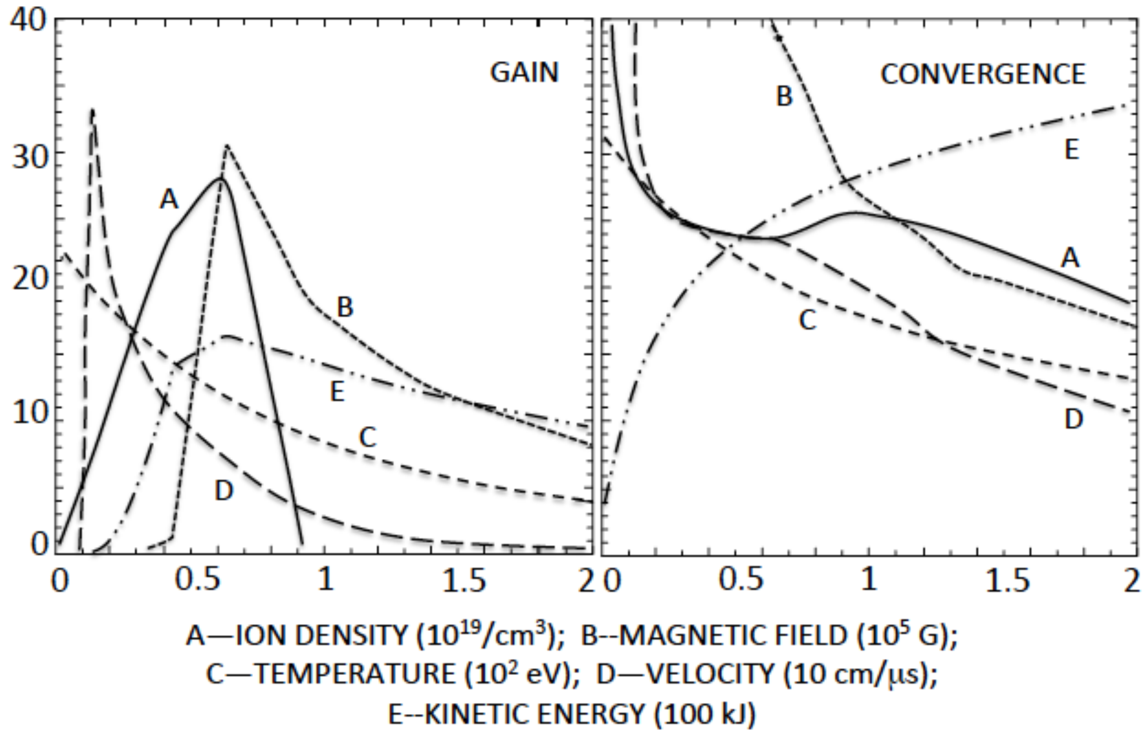


Fig. 13. The variation of gain (left) and convergence ratio (right) with variation in initial parameters for a basic spherical target parameter set of $n$=2.96 x $10^{18}$/cm$^3$, $T$=31.1 eV, $B_\varphi$=106 kG, $R$=0.74 cm, $v$=3 cm/μs, $E$=60 kJ (case S.5).

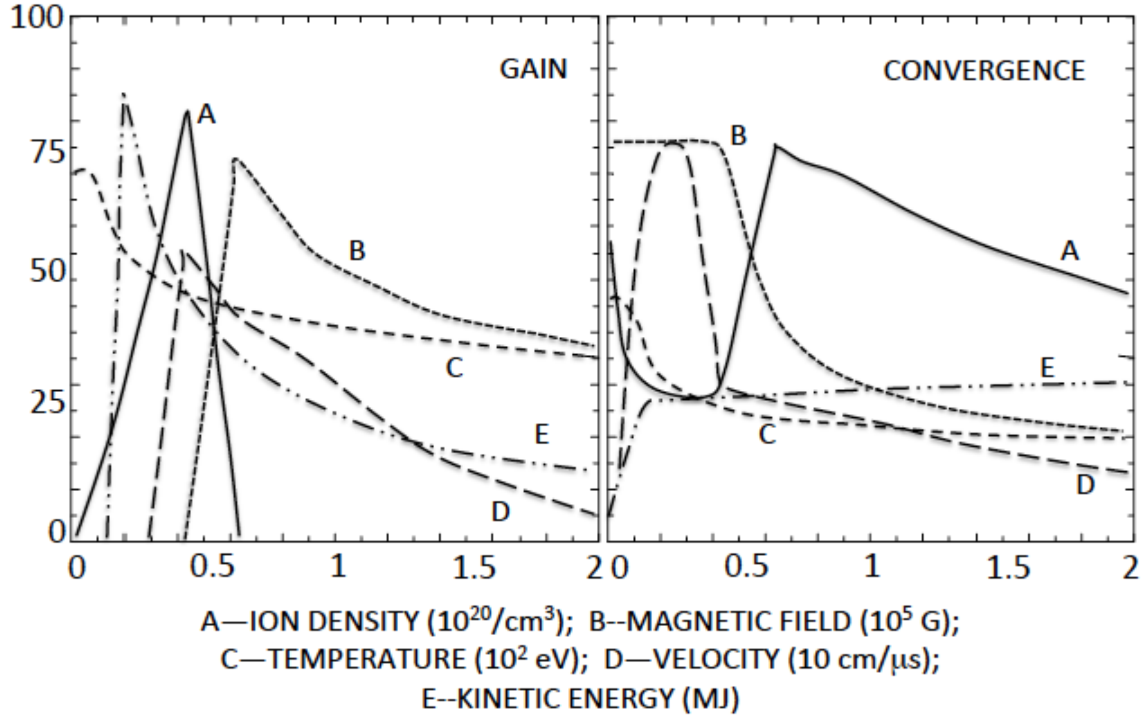


Fig. 14. The variation of gain (left) and convergence ratio (right) with variation in initial parameters for a basic spherical target parameter set of $n$=2.96 x $10^{19}$/cm$^3$, $T$=31.1 eV, $B_\varphi$=106 kG, $R$=0.65 cm, $v$=5 cm/μs, $E$=400 kJ (case S.6). Calculations that reach a convergence of 75 are arbitrarily terminated at that point.

The initial density, temperature, magnetic field, and energy-to-mass ratio of case S5 are in the range of the simulations of Knapp and Kirkpatrick[30] (K&K-14), although the mass and energy for K&K-14 are approximately 370 times larger than S5. For parameters more appropriate for the K&K-14 simulations ($n$=4.26 x $10^{18}$/cm$^3$, $T$=80 eV, $R$=4.06 cm, $B$=100 kG, $v$=6 cm/μs, $E$=22 MJ), the model of this paper gives a gain of 16, a convergence of 15.3, and a peak ion temperature of 126 keV. K&K-14 report a gain of 12.56, a maximum compression of "about 17," and a cold-fuel layer peak ion temperature that "exceeded 80 keV." K&K-14 included a cold-fuel layer, which, of course, our model does not include, but they do not discuss how much of the yield came from the cold fuel.

Fig. 12 shows that all cases considered (S.1-6) not only meet the postulated size, magnetic field, and energy limitations for $C_R$=15, they also meet the postulated limitations for $C_R$=7 (0.014-1.4 cm compressed size, 24.5 MG compressed field, 500 kJ at ignition). For projected ignition at $C_R$=7, projecting back from 7 keV leads to initial radii that are 7/15 of the radii tabulated in Table XVIII, initial magnetic fields that are $(15/7)^2$ larger, initial densities that are $(15/7)^3$ larger, and an initial temperature that is $(15/7)^{4/3}$ larger, i.e., 143 eV. The $C_R$=7 initial conditions corresponding to cases S.4, 5, and 6 are tabulated in Table XX-top, where the ignition conditions are also replicated from Table XVIII. The results of calculations using those initial values are shown in Table XX-bottom. The values when ignition is reached and the maximum values are comparable to those in Table XIX, but the ignition convergences are less than 10 and the maximum convergences are less than 12.

| Ignition conditions | | | | | | | | Initial conditions | | | | |
|---|---|---|---|---|---|---|---|---|---|---|---|---|
| Case | $n$ | $B_\varphi$ | $R$ | $RB$ | $M$ | $E_{ig}$ | $\beta$ | $n$ | $\rho$ | $B_\varphi$ | $R$ | $\beta$ |
| S.4a | $10^{21}$ | 7.51 | 0.16 | 1.20 | 0.073 | 69.8 | 10 | $2.92 \times 10^{18}$ | $1.21 \times 10^{-2}$ | 0.153 | 1.13 | 1.43 |
| S.5a | $10^{22}$ | 23.7 | 0.049 | 1.16 | 0.021 | 19.6 | 10 | $2.92 \times 10^{19}$ | 0.121 | 0.485 | 0.344 | 1.43 |
| S.6a | $10^{23}$ | 23.7 | 0.044 | 1.04 | 0.144 | 119.0 | 100 | $2.92 \times 10^{20}$ | 1.21 | 0.485 | 0.305 | 14.3 |

| | Initial | | At ignition | | | | | Maximum | | | | | |
|---|---|---|---|---|---|---|---|---|---|---|---|---|---|
| Case | $v$ | $E$ | $n$ | $B_\varphi$ | $RB$ | $T_i$ | $C_R$ | $n$ | $B_\varphi$ | $RB$ | $T_i$ | $C_R$ | Gain |
| S.4a | 1 | 200 | $1.68 \times 10^{21}$ | 9.98 | 1.36 | 6.53 | 8.31 | $5.44 \times 10^{21}$ | 20.7 | 1.96 | 44.4 | 12.0 | 15.1 |
| S.5a | 3 | 60 | $1.43 \times 10^{22}$ | 28.6 | 1.25 | 7.05 | 7.88 | $4.30 \times 10^{22}$ | 59.5 | 1.80 | 42.5 | 11.4 | 13.4 |
| S.6a | 5 | 400 | $2.52 \times 10^{23}$ | 39.3 | 1.26 | 6.24 | 9.52 | $3.96 \times 10^{23}$ | 52.9 | 1.46 | 105 | 11.1 | 48.8 |

Table XX. Targeted ignition conditions and corresponding initial conditions ($C_R = 7$; top) and computed initial, ignition, and maximum conditions (bottom) for high-gain, low convergence spherical targets with azimuthal magnetic field ($B_\varphi$) and an initial temperature of 143 eV. Units: $n$—/cm$^3$; ρ—mg/cm$^3$; $B_\varphi$—MG; $T$--keV; $R,L$—cm; $RB$—Mg-cm; $v$—cm/us; fuel mass $M$—mg; $E$—MJ.

As was the case with cylindrical $B_\varphi$ targets (Fig. 7), Fig. 11 shows that the minimum ignition size for the spherical targets decreases with increased temperature, albeit with an increase in magnetic field at the same $\beta$. Table XXI summarizes calculations that used initial conditions projected back from an ignition temperature of 15 keV. Cases S.7-10 have the same ignition density and $\beta$ and the same initial density and $\beta$ as cases S.3-6, respectively. A comparison of the corresponding cases, e.g., S.3 and S.7, reflects the smaller size and lower energy that results from targeting 15 keV as the ignition temperature. However, as was the case with the cylindrical $B_\varphi$ targets, the achievable gain is somewhat lower, so, at least based upon these calculations, there appears to be no major benefit from targeting 15 keV.

| Ignition conditions | | | | | | | | Initial conditions | | | | |
|---|---|---|---|---|---|---|---|---|---|---|---|---|
| Case | $n$ | $B_\varphi$ | $R$ | $RB$ | $M$ | $E_{ig}$ | $\beta$ | $n$ | $\rho$ | $B_\varphi$ | $R$ | $\beta$ |
| S.7 | $10^{20}$ | 11.0 | 0.065 | 0.72 | $4.77\text{x}\ 10^{-5}$ | 2.3 | 1 | $2.96\text{x}10^{16}$ | $1.24\text{x}10^{-4}$ | 0.049 | 0.97 | 0.067 |
| S.8 | $10^{21}$ | 11.0 | 0.062 | 0.68 | $4.20\ \text{x}\ 10^{-4}$ | 8.6 | 10 | $2.96\text{x}10^{17}$ | $1.24\text{x}10^{-3}$ | 0.049 | 0.93 | 0.67 |
| S.9 | $10^{22}$ | 34.8 | 0.019 | 0.66 | $1.20\text{X}10^{-3}$ | 2.4 | 10 | $2.96\text{x}\ 10^{18}$ | 0.0124 | 0.155 | 0.29 | 0.67 |
| S.10 | $10^{23}$ | 34.8 | 0.018 | 0.63 | $1.03\text{x}10^{-2}$ | 18.3 | 100 | $2.96\text{x}\ 10^{19}$ | 0.124 | 0.155 | 0.27 | 6.7 |

| | Initial | | At ignition | | | | | Maximum | | | | | |
|---|---|---|---|---|---|---|---|---|---|---|---|---|---|
| Case | $v$ | $E$ | $n$ | $B_\varphi$ | $RB$ | $T_i$ | $C_R$ | $n$ | $B_\varphi$ | $RB$ | $T_i$ | $C_R$ | Gain |
| S.7 | 0.5 | 15 | $1.22\text{x}10^{20}$ | 11.9 | 0.72 | 21.8 | 16.0 | $5.58\text{x}10^{20}$ | 32.7 | 1.19 | 69 | 26.6 | 0.26 |
| S.8 | 2 | 30 | $1.11\text{x}10^{21}$ | 11.2 | 0.67 | 14.8 | 15.5 | $6.21\text{x}10^{21}$ | 35.3 | 1.20 | 58 | 27.6 | 2.03 |
| S.9 | 2 | 6 | $3.34\text{x}10^{22}$ | 60.0 | 0.78 | 12.4 | 22.4 | $6.86\text{x}10^{22}$ | 106 | 0.98 | 37 | 26.5 | 7.65 |
| S.10 | 7.5 | 40 | $2.89\text{x}10^{23}$ | 59.1 | 0.75 | 10.2 | 21.4 | $6.26\text{x}10^{23}$ | 98.2 | 0.96 | 60 | 27.7 | 22.5 |

Table XXI. Targeted ignition conditions and corresponding initial conditions ($C_R$ = 15, $T$=15 keV; top) and computed initial, ignition, and maximum conditions (bottom) for spherical targets with azimuthal magnetic field ($B_\varphi$) and an initial temperature of 67 eV. Units: $n$—/cm$^3$; ρ—mg/cm$^3$; $B_\varphi$—MG; $T$--keV; $R$—cm; $RB$—Mg-cm; $v$—cm/us; fuel mass $M$—mg; $E$—kJ.

L&K-83 did not explicitly identify minimum conditions, although such can in principle be identified by examination of the figures and tables in the article. The approach here is to project backward from minimum ignition conditions to pick a set of initial conditions. In cases where a low gain has been computed (e.g., S.1, 2, 3), the L&K-83 results suggest that the gain can be somewhat increased by an energy substantially above the minimum value used, with a corresponding increase in size, e.g., initial radius, although high gain does not appear possible at such low values of initial density.

L&K-83 noted that "at a fixed point in the ($\rho_o$,$v_o$) plane, whether or not alpha deposition is advantageous depends on the location of the point, and, in fact, we have observed points in the new parameter space where the gain actually decreases slightly if $f_d$=1 instead of $f_d$=0." To emphasize this point, using the present model we have recomputed the point $E_o$=1 MJ, $M$=0.2 mg, $T_o$=50 eV, $B_o$=40 kG, $v_o$=1.6 cm/μs, $\rho_o$=4 x 10$^{-6}$ g/cm$^3$. Table III of L&K-83 indicated a gain of 26 without alpha deposition, even when the computation was terminated at the "free-fall" condition. Without such a termination the gain increases to 30, albeit at a convergence of 40. With the more complete present model, the gain is reduced to 19.3 at a maximum convergence of 28 because the fuel pressure increases more rapidly due to alpha deposition.

The present model can also essentially invalidate some of the L&K-83 results. For example, in Table V, L&K-83 show that the point $E$=1 MJ, $M$=0.2 mg, $T$=50 eV, $B$=40 kG, $v$=10 cm/μs, $\rho$=1.6 x 10$^{-3}$ g/cm$^3$ reaches a gain of 40.1. In the context of the present model, a gain of 42 is achieved at a convergence of 32.5 without the thermoelectric effect. However, when the thermoelectric effect is included, the magnetic flux is depleted so rapidly that the gain is below unity at a convergence of 50. Nevertheless, for the most part, the results of L&K-83 remain qualitatively valid.

Because of the driver and plasma formation technology available then, L&K-83 focused on an energy of 10 kJ, an initial temperature of 40 eV, and an initial magnetic field of 40 kG, values which can be substantially exceeded with present technology. L&K-83 also focused on the "new G>1 region," although several figures clearly showed a continuum between the new region and the conventional unmagnetized target region, i.e., Magnetized Target Fusion covers a wide range in density and velocity space and is not limited to the low-density, low-velocity region.

For the high-gain spherical targets considered in this section, the initial target plasmas have an initial density range of $3 \times 10^{17}$-$3 \times 10^{20}/cm^3$, an initial $\beta$ range of 0.7-14, and an initial temperature of 31-143 eV. Ignition conditions, without high gain, were reached with initial densities up to a factor of $10^3$ lower. The high-gain density range includes the high-gain range of the $B_\varphi$ cylindrical targets and reaches the lower density values of the $B_z$ cylindrical targets. A major difference is that the initial temperature for the spherical targets is significantly lower. In principle, the lower temperature requirement reduces the difficulty in developing a target plasma formation system, although the spherical geometry adds greater difficulty compared to cylindrical geometry. Regardless, the development of the appropriate target plasma with the appropriate density is a major challenge of MTF.

From a driver perspective, the highest energy for the spherical targets (400 kJ) is the lowest considered for the cylindrical targets. The velocity range for high gain (1-5 cm/μs) is higher than required for high gain with $B_\varphi$ cylindrical targets and lower than the highest values required for $B_z$ cylindrical targets. As with the $B_\varphi$ cylindrical targets, the spherical targets offer the possibility of high gain at a convergence less than 15.

## VII. SUMMARY AND CONCLUDING REMARKS

In this paper, we have extended a simple magnetized target implosion model to survey the potential parameter space in which three types of magnetized targets—cylindrical $B_z$ , cylindrical $B_\varphi$, and spherical $B_\varphi$—might achieve ignition and produce large gain at achievable radial convergence ratios. We have used the model to compute the behavior of many parameter sets and have shown gains greater than 30 can potentially be achieved for all geometries.

Projecting backward from the ignition conditions, i.e., density-size-magnetic field-temperature combinations where the fusion energy deposition rate equals the sum total of conduction and radiation loss rates, we have defined a set of initial conditions (*n*-*R*-*B*-*T*) and implosion conditions (*v,E*) whereby high gain can be reached. A major result of this paper is that each type of target operates in a different initial density-energy-velocity range. The cylindrical $B_z$ targets operate at relatively high initial density (e.g., $10^{21}/\text{cm}^3$), relatively smaller initial size (< 5mm) and relatively high velocity (e.g., 10 cm/μs), albeit at lower density and velocity than conventional unmagnetized targets. In contrast, the cylindrical $B_\varphi$, targets operate a relatively low initial density (e.g., $10^{18}/\text{cm}^3$), relatively larger initial sizes (e.g., 5 cm), and relatively low velocity (e.g., 0.5 cm/μs), but in comparable energy range (e.g., 1 MJ) and magnetic field range (e.g., 300 kG). The initial size, initial density and velocity of spherical targets span much of that for the other two types of targets, but the initial temperature, initial magnetic field and shell kinetic energy can be significantly lower. We have shown that high gain may be obtained at extremely low convergence ratios, e.g., less than 15.

The initial conditions, driver requirements and computed fusion gain of the calculations discussed in this paper are summarized in Table XXII. These results can be used as a basic guide for MTF plasma formation system and driver development. However, these results are probably not completely inclusive of the parameter space where high gain can be achieved. For example, we have considered primarily cases that are projected to reach the minimum size at ignition. Many cases considered in this paper have required ignition energies or minimum size below our postulated limits, so the same initial density, temperature and magnetic field could be considered at a larger size. The L&K-83 results where the energy was increased while keeping the energy-to-mass ratio fixed suggest that somewhat higher gain may be achieved if the mass used is greater than the minimum required for ignition. Of course, any plasma system that has thermal losses less than the model used in this paper can potentially achieve ignition in a different parameter space. Magnetically confined plasmas, i.e., plasmas not in contact with a cold surface, in principle have no thermal losses but must contend with instabilities that potentially put them in contact with a cold surface.

| | Type | Cyl. $B_z$ | Cyl. $B_z$ Low $C_R$ | Cyl. $B_\varphi$ Low Gain | Cyl. $B_\varphi$ | Cyl. $B_\varphi$ Low $C_R$ | Sphere Low Gain | Sphere | Sphere Low $C_R$ |
|---|---|---|---|---|---|---|---|---|---|
| | gain | 16-30 | 12-23 | < 2 | 10 | 30 | <2 | 16-75 | 13-50 |
| | $C_R$ | 24-30 | 17-19 | 27-31 | 27 | 12 | 23-26 | 25-29 | 11-12 |
| Initial Conditions | mass M(mg) | 0.2-0.6 | 0.5-0.6 | 0.01-0.2 | 0.6 | 1.56 | 0.005-0.09 | 0.02-0.144 | 0.2-0.144 |
| | $R$ (cm) | 0.15-0.46 | 0.21-0.34 | 2.3-8.7 | 2.15 | 5 | 2.6-9.9 | 0.65-2.4 | 0.3-1.1 |
| | $L$ (cm) | 0.5-1.5 | 1-1.7 | 2.3-8.7 | 2.2 | 2 | -- | -- | -- |
| | $n$ (/cm$^3$) | 1.3x10$^{20}$-4.5x10$^{21}$ | 2x10$^{20}$-10$^{21}$ | 4.5x10$^{15}$-4.5x10$^{17}$ | 4.5 x 10$^{18}$ | 2.4 x 10$^{18}$ | 3x10$^{14}$-3x10$^{16}$ | 3x10$^{17}$-4x10$^{19}$ | 3x10$^{18}$-3x10$^{20}$ |
| | $B$ (kG) | 180-330 | 475-488 | 160-500 | 500 | 300 | 11-33 | 106 | 150-485 |
| | $T$ (eV) | 250 | 400 | 189 | 189 | 500 | 31 | 31 | 143 |
| Driver Requirements | $v$ (cm/μs) | 4-15 | 3.5-7 | 0.15-0.4 | 1 | 0.3 | 0.1-0.6 | 1-5 | 1-5 |
| | $E$ (MJ) | 0.6-3 | 2 | 0.4-2 | 2 | 4 | 0.08-0.3 | 0.06-0.4 | 0.06-0.4 |
| | $E/M$ (MJ/mg) | 1.8-4.9 | 3.5-4.1 | 1.5-36.4 | 3.51 | 2.56 | 9-60 | 2.7-2.9 | 2.7-2.9 |

Table XXII. Summary of target calculations discussed in this paper.

We have shown that reaching ignition conditions does not necessarily lead to high gain and high fuel burn-up. At the lower densities whereby fusion temperatures can be reached in magnetized targets, the fusion burn rate may be only comparable to the hydrodynamic heating/cooling rates. On the other hand, when the fusion burn rates significantly exceed the hydrodynamic rates, we show a characteristic rapid increase in temperature with a subsequent increased burn rate and high gain.

We have not addressed the issue of whether or not initial plasmas having the required initial characteristics can actually be formed within an implodable system. The results of this paper (Table XXII) suggest that plasmas for spherical, $B_\varphi$ cylindrical, and $B_z$ cylindrical targets must have an initial density greater than approximately $10^{17}$/cm$^3$, $10^{18}$/cm$^3$, and $10^{20}$/cm$^3$, respectively. Section I mentions some of the approaches that are currently being investigated for forming a magnetized plasma. MAGO-like (references 13 and 28) electrical discharges produce magnetized plasmas in the $10^{18}$/cm$^3$ range that is near-optimum for cylindrical $B_\varphi$ and spherical targets (Table XXII). MagLIF uses lasers to form a plasma in the $10^{20}$/cm$^3$ range in a volume that has an initial magnetic field present. Laser beat waves have been proposed as a way to magnetize a preformed, unmagnetized plasma and have the potential of covering a wide density range.[31] The Sandia Φ-targets (references 3 and 4) used a non-relativistic electron beam to create a voltage that induced an electrical discharge.

We have also not addressed the issue of whether or not the hot, magnetized plasmas resulting from the implosion of magnetized fuel can be used as a central "ignitor" to ignite "cold" fuel, leading to substantially higher gain. The calculations of Lindemuth and Kirkpatrick (reference 19), S&V-12, and K&K-14 suggest that this may be possible at the higher end of the MTF density spectrum, e.g., the S&V-12 simulations showed gains as high as 1000 for an initial fuel density in the range of 1.2 x $10^{21}$/cm$^3$ (5 mg/cm$^{3)}$. However, such high gain may not be possible at the lower end of the density spectrum because of the lower burn rates. An examination of this issue is left for future work. Regardless, implementing a cold fuel layer in a target plasma formation system would appear to be a more formidable challenge than developing the target plasma in the first place.

We also have not addressed whether or not an imploding shell having the required characteristics can be developed. In that regard, calculations using a more complete shell model, including, e.g., a realistic drive history, and a more complete target model could validate or modify somewhat the velocity-energy requirements determined with the simplified implosion model of this paper.

We have postulated practical size and energy limitations that are consistent with current work in magnetically driven imploding liners. We also have shown that the velocity, energy, and convergence required span the range that has either already been demonstrated in the current work in magnetically driven liners or is potentially attainable with near term upgrades. We note that liners in the lower velocity range can, in principle, be solid or liquid, whereas at the higher velocities, the liner, if magnetically driven, will be plasma. We also note that at a given energy level, higher velocity means lower shell mass, a potentially important reactor consideration. We have not addressed such issues as imploding shell stability, a significant issue as discussed by Slutz-10, S&V-12, and Sefkow et al.[32] The present state of liner research appears to be closer to MTF's requirements than the present state of magnetized plasma formation research.

MTF is based upon the premise of classical, or near classical, reduction in thermal conduction because of the magnetic field, although Slutz-10 and L&S-09 suggest that MTF may work even with Bohm transport. Bohm transport may be a concern particularly for cases Φ1-4 of Section V and cases S1-3 of section VI, all of which have an initial $\beta$ much less than unity. These are low gain cases and are not as likely to be of as much interest as the high-gain cases, all of which have an initial $\beta$ approaching unity. Of course, for all cylindrical $B_\varphi$ and spherical cases the $\beta$ increases during the implosion process (Table III). An accurate evaluation of the effect of Bohm transport requires detailed implosion calculations using Bohm transport coefficients. This is left for future work.

In the relatively wide density-temperature-field space identified in this paper, there is little experimental data confirming an adequate reduction of thermal losses by a magnetic field, and there is very limited data on plasma behavior under the wide range of implosion conditions considered. Furthermore, ignition in MTF is based upon the premise that the magnetic field can enhance alpha deposition, another premise not confirmed experimentally. In this regard, the MagLIF experiment indicate that the deposition of triton energy was significantly enhanced by the magnetic field, and the Larmor radius of tritons is very similar to that of an alpha particle. The fundamental premises of MTF can, in principle, be confirmed with existing or near term drivers, e.g., magnetically imploded liners, perhaps driven by explosively driven flux compression generators. Confirmation of these premises, and a determination of whether or not our present understanding of magnetized plasma physics is adequate, is a prerequisite for design of reactors and reactor technology based on MTF.

As the PCAST[33] has noted, in a different context, "producing an ignited plasma will be a truly notable achievement for mankind and will capture the public's imagination. Resembling a burning star, the ignited plasma will demonstrate a capability with immense potential to improve human well-being. Ignition is analogous to the first airplane flight or the first vacuum-tube computer. As in those cases, the initial model need not resemble the one that is later commercialized."

Magnetized Target Fusion (MTF) is an emerging field of research rich in possibilities for physics discoveries and contributions to fundamental science. As an energy research program, it is orthogonal to and complementary to conventional magnetic confinement and inertial confinement research. Because MTF is qualitatively different from inertial or magnetic confinement—different time, length, density, and yield scales—MTF reactors will have different characteristics and trade-offs, increasing the chances that a practical fusion power scheme can be found. As with L&K-83, "the main message of this paper: magnetized fuel targets represent the possibility of attaining significant fuel burn, with driver requirements reduced by several orders of magnitude below the levels currently being considered in conventional target design."

## ACKNOWLEDGEMENTS

R. C. (Ron) Kirkpatrick's original insight on the usefulness of simple target models, and technical discussions with him over more than three decades, has provided the foundation for this work. R. E. (Dick) Siemon's original analytic insight into the role of density in fusion, and the number of workshops he organized and the number of seminars he presented in the late 1990s and early 2000s, are at least in part responsible for the present interest in Magnetized Target Fusion (MTF) and for this work. S. A. (Steve) Slutz has made useful comments that have strengthened this paper and has encouraged the publication of this work and a previous paper (L&S-09).

## REFERENCES

[1] I. R. Lindemuth and R. E. Siemon, Am. J. Phys. **77**, 407 (2009).
[2] I. R. Lindemuth and R. C. Kirkpatrick, Nucl. Fusion **23**, 263 (1983).
[3] Phys. Today **30**, 17 (1977); J. N. Olsen, M. M. Widner, J. Chang, and L. Baker, J. Appl. Phys. **50**, 3224 (1979).
[4] M. A. Sweeney and A. V. Farnsworth, Nucl. Fusion **21**, 41 (1981).

[5] J. H. Degnan, D. J. Amdahl, M. Domonokos, F. M. Lehr, Nucl. Fusion **53**, 093003 (2013).
[6] J. P. Knauer, O. V. Gotchev, P. Y. Chang, D. D. Meyerhofer, O. Polomarov, R. Betti, J. A. Frenje, Phys. Plas. **17**, 056318 (2010).
[7]M. R. Gomez, S. A. Slutz, A. B. Sefkow, D. B. Sinars, K. D. Hahn, S. B. Hansen, E. C. Harding, P. F. Knapp, P. F. Schmit, C. A. Jennings, T. J.Awe, M. Geissel, D. C. Rovang, G. A. Chandler, G. W. Cooper, M. E. Cuneo, A. J. Harvey-Thompson, M. C. Herrmann, M. H. Hess, O. Johns, D. C. Lamppa, M. R. Martin, R. D. McBride, K. J. Peterson, J. L. Porter,G. K. Robertson, G. A. Rochau, C. L. Ruiz, M. E. Savage, I. C. Smith, W. A. Stygar, and R. A. Vesey, Phys. Rev. Lett. 113, 155003 (2014).
[8] P. F. Schmit, P. F. Knapp, S. B. Hansen, M. R. Gomez, K. D. Hahn, D. B. Sinars, K. J. Peterson, S. A. Slutz, A. B. Sefkow, T. J. Awe, E. Harding, C. A. Jennings, G. A. Chandler, G. W. Cooper, M. E. Cuneo, M. Geissel, A. J. Harvey-Thompson, M. C. Herrmann, M. H. Hess, O. Johns, D. C. Lamppa, M. R. Martin, R. D. McBride, J. L. Porter, G. K. Robertson, G.A. Rochau, D. C. Rovang, C. L. Ruiz, M. E. Savage, I. C. Smith, W. A.Stygar, and R. A. Vesey, Phys. Rev. Lett. 113, 155004 (2014).
[9] S. A. Slutz, M. C. Hermann, R. A. Vesey, A. B. Sefkow, D. B. Sinars, D. C. Rovang, K. J. Peterson, and M. E. Cuneo, Phys. Plasmas **17**, 056303 (2010).
[10] S. C. Hsu, T. J. Awe, S. Brockington, A. Case, J. T. Cassibry, G. Kagan, S. J. Messer, M. Stanic, X. Tang, D. R. Welch, F. D. Witherspoon, IEEE Trans. Plasma Sci. **40**, 1287 (2012).
[11] M. Laberge, J. Fusion Energy **27**, 65 (2008).
[12] L. J. Perkins, B. G. Logan, G. B. Zimmerman, and C. J. Werner, Phys. Plasmas **20**, 072708 (2013).
[13] O. M. Burenkov, Y. N. Dolin, P. V. Duday, V. I. Dudin, V. A. Ivanov, A. V. Ivanovsky, G. V. Karpov, A. I. Kraev, V. B. Kudelkin, V. I. Mamyshev, I. V. Morozov, S. V. Pak, S. M. Polushko, A. N. Skobelev, and V. A. Tokarev,“New configuration of experiments for MAGO program,” in 14th International Conference on Megagauss Magnetic Field Generation and Related Topics (edited by G. F. Kiuttu, K. W. Struve, J. H. Degnan), IEEE, New York, NY, ISNB 978-1-4673-5719-7, 119 (2012).
[14] X. J. Yang, H. Zhang, Z. W. Dong, “The effect of the strong magnetic field on the process of ignition in the magnetized plasma,” in 14th International Conference on Megagauss Magnetic Field Generation and Related Topics (edited by G. F. Kiuttu, K. W. Struve, J. H. Degnan), IEEE, New York, NY, ISNB 978-1-4673-5719-7, 148 (2012).
[15] National Nuclear Security Administration’s Path Forward to Achieving Ignition in the Inertial Confinement Fusion Program: Report to Congress, December 2012; NNSA, US Department of Energy, Washington DC.
[16]http://arpa-e.energy.gov/sites/default/files/documents/files/ALPHA%20Project%20Descriptions_FINAL.pdf for awardee institutions, award amounts, and project descriptions.
[17] G. A. Wurden, S. C. Hsu, T. P. Intrator, T. C. Grabowski, J. H. Degnan, M. Domonokos, P. J. Turchi, E. M. Campbell, D. B. Sinars, M. C. Hermann, R. Betti,B. S. Bauer, I. R. Lindemuth, R. E. Siemon, R. L. Miller, M. Laberge, and M. Delage, “Magneto- Inertial Fusion,” J. Fusion Energy (published online 2015).
[18] I. R. Lindemuth and R. C. Kirkpatrick, Atomkernenergie/Kerntechnik **45**, 9 (1984).

[19] I. R. Lindemuth and R. C. Kirkpatrick, Fusion Tech. **20**, 829 (1991).
[20] S. A. Slutz and R. A. Vesey, Phys. Rev. Lett. **108**, 025003-1 (2012).
[21] W. T. Armstrong and J. A. Morgan, "Liner compression of magnetically confined FRC plasmas," in 4th International Conference on Megagauss Magnetic Field Generation and Related Topics (edited by C. M. Fowler, R. S. Caird, D. J. Erickson), Plenum, New York, NY, ISNB 0-306-42574-2, 683 (1987).
[22] R. D. McBride and S. A. Slutz, Phys. Plasmas **22**, 052708 (2015).
[23] S. I. Braginskii, *Reviews of Plasma Physics* (Consultants Bureau, New York, 1965), Vol. 1, P. 205.
[24] J. D. Lindl, Phys. Plasmas **2**, 3933 (1995).
[25] J. J. Duderstdat and G. A. Moses, *Inertial Confinement Fusion* (John Wiley and Sons, New York, 1982).
[26] M. M. Basko, A. J. Kemp, J. Meyer-ter-Vehn, Nucl. Fusion **40**, 59 (2000).
[27] I. R. Lindemuth, J. S. Pettibone, J. C. Stevens, R. C. Harding, D. M. Kraybill, and L. J. Suter, Phys. Fluids. **21**, 1723 (1978).
[28] I. R. Lindemuth, R. E. Reinovsky, R. E. Chrien, J. M. Christian, C. A. Ekdahl, J. H. Goforth, R. C. Haight, G. Idzorek, N. S. King, R. C. Kirkpatrick, R. E. Larson, G. L. Morgan, B. W. Olinger, H. Oona, P. T. Sheehey, J. S. Shlachter, R. C. Smith, L. R. Veeser, B. J. Warthen, S. M. Younger, V. K. Chernyshev, V. N. Mokhov, A. N. Demin, Y. N. Dolin, S. F. Garanin, V. A. Ivanov, V. P. Korchagin, O. D. Mikhailov, I. V. Morozov, S. V. Pak, E. S. Pavlovskii, N. Y. Seleznev, A. N. Skobelev, G.I. Volkov, and V. A. Yakubov, Phys. Rev. Lett. **75**, 1953 (1995).
[29] F. J. Wessel, H. Rahman, P. Ney, R. Presura, IEEE Trans. Plasma Sci. **43**, 2463 (2015).
[30] C. E. Knapp and R. C. Kirkpatrick, Phys. Plasmas **21**, 070701 (2014).
[31] D. R. Welch, T. C. Genoni, C. Thoma, D. V. Rose, and S. C. Hsu, Phys. Plasmas **21**, 032704 (2014).
[32] A. B. Sefkow, S. A. Slutz, J. M. Koning, M. M. Marinak, K. J. Peterson, and D. B. Sinars, Phys. Plasmas **21**, 072711 (2014).
[33] President's Committee of Advisors on Science and Technology (PCAST), Report on Fusion Energy (July 1995), p. 22.